PHYSICAL REVIEW FLUIDS **8**, 123801 (2023)

Biglobal analysis of baroclinic instability in a current-undercurrent oceanic system

Xianliang Chen,[1] Jianping Gan,[1,2,*] and James C. McWilliams[3]
[1] *Center for Ocean Research in Hong Kong and Macau and Department of Mathematics, The Hong Kong University of Science and Technology, Hong Kong 999077, People's Republic of China*
[2] *Department of Ocean Science, The Hong Kong University of Science and Technology, Hong Kong 999077, People's Republic of China*
[3] *Department of Atmospheric and Oceanic Sciences, University of California, Los Angeles, Los Angeles, California 90095, USA*

(Received 20 July 2023; accepted 13 November 2023; published 11 December 2023)

In this work, baroclinic instability in a current-undercurrent system is analyzed using the biglobal instability analysis (BIA). Idealized model flows are considered and the flow parameters are estimated from the Western North Pacific circulation system. Compared with the prevailing one-dimensional linear stability analysis (1D-LSA), BIA can deal with the basic flow of continuously nonuniform vertical shear and strong horizontal variation within the framework of the Boussinesq equation to account for nongeostrophic effects. The basic velocity gradually changes from the vertically linear Eady type to a more realistic distribution, which destabilizes the Phillips-type mode due to the strengthening of the vertical shear. With an increasing zonal velocity variation, the mode is more of a barotropic type in the long-wave range and is more of a baroclinic type in the short-wave range. Moreover, the high vertical shear near the vertical boundaries supports a series of Charney-type modes in the confined boundary region. The Charney modes are severely affected by the boundary constraint, leading to a wide unstable wave-number range deep into the small-scale region and enhanced ageostrophic motions. The top and bottom boundary layers due to viscosity and diffusivity can be destabilizing and sustain the modal growth for short waves. In comparison, 1D-LSA can overestimate the growth rate of baroclinic modes and cannot quantify the coupling effects with the horizontal shear for the present case.

DOI: 10.1103/PhysRevFluids.8.123801

I. INTRODUCTION

A prominent feature of oceanic flows is that they cover vast ranges of temporal and spatial scales. Nevertheless, most of the kinetic energy resides in mesoscale eddies [1], whose horizontal scales are typically ∼10 to ∼100 km with Rossby numbers (Ro) smaller than unity. These energetic eddies play significant roles in transporting mass, heat, and biogeochemical components [2]. It is generally accepted that most mesoscale eddies are initially driven by a mechanism called baroclinic instability, which occurs in vertically sheared, rotating stratified flows [3]. The available potential energy related to buoyancy gradients serves as the source of eddy kinetic energy [4]. Furthermore, baroclinically unstable waves are capable of inducing sizable vertical buoyancy fluxes and thus crucial in the restratification process in oceanic mixed layers [5]. Therefore, baroclinic instability has long been one of the most important problems in geophysical fluid dynamics, earning wide focus in theoretical, modeling, and observational investigations. Though investigated extensively, baroclinic instability

---

[*] Corresponding author: magan@ust.hk

deserves a revisit to explore further its behavior in realistic multidimensional and complex flow systems.

Early pioneering works on baroclinic instability were accomplished by Charney [6], Eady [7], and Phillips [8]. Different model problems were established using a mean flow of either uniform vertical shear or multilayers, based on which linear stability analysis (LSA) was conducted. It is found that there is a dominant geostrophic mode, associated with the sign change of the potential vorticity gradient (see Refs. [9,10] for the full Charney-Stern-Pedlosky (CSP) condition). This mode is successful in explaining the scales and growth rates of the disturbances commonly observed. Afterwards, Stone [11] (also Tokioka [12]) extended Eady's results to account for nongeostrophic, or ageostrophic, effects, and found extra unstable modes beyond the short-wave cutoff. These ageostrophic modes are classified into at least three types: convective mode, symmetric mode, and inertial critical layer (ICL) mode, where the Richardson number (Ri) is crucial for the classification. The geostrophic mode is nearly balanced in an extensive range of Ro, while ageostrophic modes are highly unbalanced [13]. Ageostrophic modes are active on small scales, so they are crucial in inducing submesoscale motions [14]. Although various types of ageostrophic modes have been identified [11,13,15], a complete physical picture is still lacking. In addition to idealized model flows, baroclinic instability in real oceans has also been widely analyzed using observational or numerical data. For example, Qiu [16] applied LSA on satellite-measured mean flows and successfully explained the seasonal variation of the growth rate of mesoscale eddies in the North Pacific subtropical countercurrent. Smith [17] demonstrated that nearly the entire ocean was linearly unstable. In low-latitude regions, the instability is more dominated by surface intensified modes, while at higher latitudes, the instability is more due to the thermocline depth shears. Furthermore, the timescale is well approximated by the Eady estimate, while the spatial scale has an apparent deviation. Recently, by using LSA, Feng *et al.* [18] provided a view of how four types of baroclinic instability were distributed in global oceans.

The starting point of this work is from the methodology view of LSA. The prevailing way of analyzing baroclinic instability is the local one-dimensional (1D) LSA, where the disturbance $\tilde{q}'$ (velocity, buoyancy, or others) is assumed periodic temporally and spatially except in the vertical direction,

$$\tilde{q}' = \hat{q}'_{1\mathrm{D}}(z)\exp[i(-\omega t + k_x x + k_y y)]. \tag{1}$$

Here $\hat{q}'$ is the shape function, z is the vertical coordinate, and x and y are the horizontal ones; ω, k_x, and k_y are the disturbance circular frequency and two horizontal wave numbers. We consider meridional flows on the f plane here. To match the 1D assumption of $\hat{q}'_{1\mathrm{D}}$, only vertical variations of the basic flow velocity $\bar{V}$ and buoyancy frequency N^2 are considered. If the primitive or the Boussinesq equations are needed to account for ageostrophic effects, then the thermal-wind relation poses an additional restriction that $\bar{V}(z)$ is a linear function of z for the solution of Eq. (1) (see Sec. II B for more details), adopted since Eady's model. Nevertheless, a linear distribution of $\bar{V}(z)$ can be largely different from realistic oceanic flows. As a simplification, the restriction of linearity is relaxed in some works by artificially dropping several terms in the basic flow and disturbance equations (see, e.g., Refs. [15,19]). The 1D quasigeostrophic (QG) LSA can deal with $\bar{V}(z)$ and $N^2(z)$ of arbitrary shapes [17,20]. Nevertheless, the "local approximation" assuming local horizontal homogeneity may have deviations when the basic flow encounters strong horizontal variations. A careful estimation on the above approximations is lacking. More importantly, as one neglects the contribution of the horizontal velocity gradient, i.e., the horizontal shear, the relative importance of baroclinic instability cannot be judged versus, e.g., the barotropic one whose major energy source is horizontal shear.

A natural thought to extend the theory availability is to utilize the 2D-LSA or biglobal instability analysis (BIA) (see the review articles of Theofilis [21,22] and the references herein). The disturbance is not restricted to be periodic in one horizontal direction, taken here to be the x direction considering the thermal wind relation between $\bar{V}(z)$ and the buoyancy field. Instead, it takes the form of

$$\tilde{q}' = \hat{q}'_{2D}(x, z) \exp[i(-\omega t + k_y y)]. \quad (2)$$

Here $\hat{q}'_{2D}$ is discretized in both the x and z directions for a global solution of the disturbance mode, and the basic flow $\bar{V}(x, z)$ can be an arbitrary 2D function. An obvious advantage is that the overall instability characteristics of the flow cross section $\bar{V}(x, z)$ can be obtained. This is especially suitable for currents with slight along-current variations, so a section-by-section analysis is feasible. Meanwhile, one can include the effects of topography with the basic flow equation strictly satisfied. Compared with the multilayer QG model which also allows a horizontally varying $\bar{V}$ [23], BIA is more generalized by allowing continuous vertical variation (mathematically, sufficient vertical levels) and including ageostrophic effects. In comparison with the direct numerical or large-eddy simulations [24], BIA is computationally cheaper and more effective in revealing the normal-mode characteristics of small-amplitude disturbances over wide wave-number ranges.

On the other hand, BIA is limited to linear normal-mode analysis and 2D basic flow. Also, the number of variables after discretization rises by a factor of N_x (grid number) over that in 1D-LSA, leading to a severe increase in computational cost. There have been some successful applications of BIA in analyzing geophysical flows. Barth [25] finished a pioneering work of employing Eq. (2) and the primitive equation to analyze the coastal jets off Northern California. The dynamics of frontal instability was investigated in detail, though a global mode spectrum was not presented due to limited computational resources. Snyder [26] designed 2D-LSA on steady fronts subject to baroclinic and Kelvin-Helmholtz instabilities. Instead of solving a large-scale global matrix of the eigenvalue problem, they directly solved the disturbance equations using a time-stepping method. Other attempts of BIA for studying coastal jets and frontal instabilities include the works of Lozier *et al.* [27], Brink [28], and Johnson and Rodney [29]. Considering the strong capability and relative obscurity of BIA, the main objective of the present work is to utilize BIA for studying baroclinic instability and ageostrophic motions based on a mean flow with nonuniform vertical shear and strong horizontal variation. The specific flow we considered is a current-undercurrent system. An undercurrent means that the lower-layer water flows in the opposite direction from the upper layer. A well-known example is the eastward Equatorial Undercurrent [30]. Undercurrents have received increasing academic interest recently, owing to their global existence, crucial roles in ocean circulation, and unique dynamical features [31]. Due to its strong vertical shear, the current-undercurrent system is subject to pronounced baroclinic instability and hence is a classic model problem [3,13,15]. As shown in Fig. 1, there are complex undercurrents in the Western North Pacific (WNP) [33,34]. A recent hotspot is the Luzon Undercurrent (LUC) flowing southward within a depth range of around 750 to 1500 m, right beneath the northward Kuroshio Current (KC) [32,35]. Currently, the dynamics of LUC are not fully understood. It is believed that barotropic and baroclinic instabilities have joint contributions and the latter is crucial in the alteration of the vertically sheared KC-LUC system and thus in the formation and maintenance of the LUC. Therefore, the present BIA on the current-undercurrent system will help understand the dynamics related to baroclinic and ageostrophic instabilities.

Observational and modeling datasets have been developed in the present authors' group for the WNP and marginal seas [36,37]. They can serve as the basic flow for BIA. Nevertheless, idealized analytical flows are adopted in this work as a first step, enabling direct comparisons with previous classic results for idealized flows. Consequently, the effects of basic-flow variations and ageostrophic motions on baroclinic instability are more easily seen. As will be shown, the flow of multiple high-vertical-shear layers can support different types of unstable modes that have unique features. The remainder of the article is organized as follows. Section II describes the basic flow and the formulation of BIA based on the Boussinesq equation. A decomposition of the disturbance growth rate is introduced to help understand the contributions of different physical terms. Different types of unstable modes are identified whose nomenclature is discussed in Sec. III. The modes are categorized following standard usage and are studied at length in Secs. IV and V. The roles

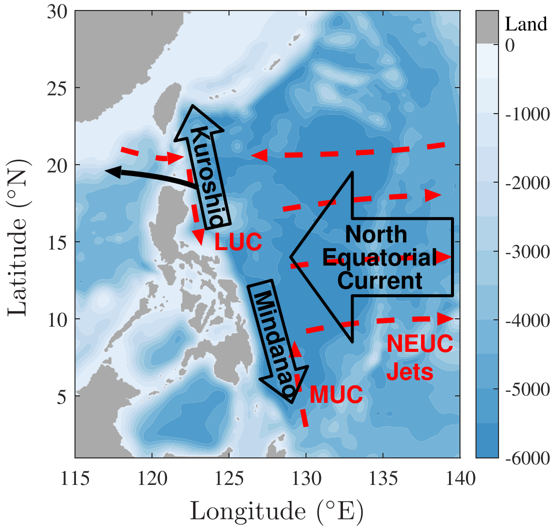

FIG. 1. Bathymetry (m) contours, and the schematic of the main upper-layer currents (black arrows) and middle-layer undercurrent system (dashed arrows) in the Western North Pacific [32]. MUC, Mindanao Undercurrent; NEUC, North Equatorial Undercurrent; KC, Kuroshio Current; LUC, Luzon Undercurrent.

of horizontal shear and ageostrophic motions are also a focus. Finally, the work is summarized in Sec. VI.

II. PROBLEM FORMULATION

A. Governing Boussinesq equation

We consider the dynamics of a nonhydrostatic rotating fluid in the Boussinesq limit on the f plane (f is the Coriolis frequency). The governing conservation equations are

$$\frac{D^*\boldsymbol{u}^*}{D^*t^*} + f^*\boldsymbol{e}_z \times \boldsymbol{u}^* = -\nabla^* p^* + b^*\boldsymbol{e}_z + \nu^*\Delta^*\boldsymbol{u}^*, \quad \nabla^* \cdot \boldsymbol{u}^* = 0, \quad \frac{D^*b^*}{D^*t^*} = \kappa^*\Delta^* b^*, \tag{3}$$

where the superscript $*$ denotes dimensional quantities; $\boldsymbol{u}$ is $[u, v, w]^T$ with u, v, and w as the zonal, meridional, and vertical velocities, respectively; and $\boldsymbol{e}_z$ is the vertical unit vector. Also p is the pressure divided by a reference density ρ_0, b^* is the buoyancy, and ν and κ are the viscosity and diffusivity. Though the viscous and diffusion terms are very small in mesoscale flows, they are included because of their significance to the disturbance growth (see Sec. II D).

Nondimensional parameters are defined as

$$(x, y) = \frac{(x^*, y^*)}{L^*}, \quad z = \frac{z^*}{H^*}, \quad t = \frac{t^* U_0^*}{L^*} = \frac{t^*}{t_0^*}, \quad (u, v) = \frac{(u^*, v^*)}{U_0^*},$$

$$w = \frac{w^* \bar{N}^{*2} H^*}{f^* U_0^{*2}} = \frac{w^*}{w_0^*}, \quad p = \frac{p^*}{\rho_0^* f^* U_0^* L^*}, \quad b = \frac{b^* H^*}{f^* U_0^* L^*}. \tag{4}$$

Here L^* and H^* are the horizontal and vertical length scales, U_0^* is the characteristic velocity, and $\bar{N}^*$ is the spatially averaged Brünt-Väisälä frequency. Consequently, the nondimensional Rossby, Froude, Reynolds, and Prandtl numbers, and the aspect ratio are obtained as

$$\mathrm{Ro} = \frac{U_0^*}{L^* f^*}, \quad \mathrm{Fr} = \frac{U_0^*}{\bar{N}^* H^*}, \quad \mathrm{Re} = \frac{U_0^* L^*}{\nu^*}, \quad \mathrm{Pr} = \frac{\nu^*}{\kappa^*}, \quad A_R = \frac{H^*}{L^*}. \tag{5}$$

TABLE I. Dimensional parameters for the benchmark case.

L^*(km)	H^* (m)	t_0^* (day)	w_0^* (m/s)	$\bar{N}^*$ (1/s)	ν^* (m^2/s)	κ^* (m^2/s)
75.0	1500	2.89	6.00×10^{-4}	2.00×10^{-3}	2.24×10^{-3}	2.24×10^{-3}

Besides, a nondimensional parameter $\varepsilon = \mathrm{Fr}^2/\mathrm{Ro}$ is defined to simplify expressions, following Molemaker *et al.* [13]. The resulting nondimensional form of Eq. (3) is

$$\begin{aligned}
\mathrm{Ro}\left(\frac{\partial}{\partial t} + u\frac{\partial}{\partial x} + v\frac{\partial}{\partial y} + \varepsilon w\frac{\partial}{\partial z}\right)u - v + \frac{\partial p}{\partial x} - \frac{\mathrm{Ro}}{\mathrm{Re}A_R^2}\frac{\partial^2 u}{\partial z^2} &= 0,\\
\mathrm{Ro}\left(\frac{\partial}{\partial t} + u\frac{\partial}{\partial x} + v\frac{\partial}{\partial y} + \varepsilon w\frac{\partial}{\partial z}\right)v + u + \frac{\partial p}{\partial y} - \frac{\mathrm{Ro}}{\mathrm{Re}A_R^2}\frac{\partial^2 v}{\partial z^2} &= 0,\\
\mathrm{Fr}^2A_R^2\left(\frac{\partial}{\partial t} + u\frac{\partial}{\partial x} + v\frac{\partial}{\partial y} + \varepsilon w\frac{\partial}{\partial z}\right)w + \frac{\partial p}{\partial z} - b &= 0,\\
\frac{\partial u}{\partial x} + \frac{\partial v}{\partial y} + \varepsilon\frac{\partial w}{\partial z} &= 0,\\
\left(\frac{\partial}{\partial t} + u\frac{\partial}{\partial x} + v\frac{\partial}{\partial y} + \varepsilon w\frac{\partial}{\partial z}\right)b - \frac{1}{\mathrm{RePr}A_R^2}\frac{\partial^2 b}{\partial z^2} &= 0.
\end{aligned} \tag{6}$$

Here $f = f^*/f^* = 1$ is omitted in the nondimensional form and the horizontal viscosity and diffusivity are neglected for the small A_R considered [38] (see Sec. II B). For later use, Eq. (6) is expressed in an operator form as $\mathcal{L}(\boldsymbol{q}) = \boldsymbol{0}$, where $\boldsymbol{q} = [u, v, w, b, p]^T$ is the basic variable set. For instability analysis, we decompose $\boldsymbol{q}$ into a mean part $\bar{\boldsymbol{q}} = [\bar{U}, \bar{V}, \bar{W}, \bar{B}, \bar{P}]^T$ and a small-amplitude disturbed part $\tilde{\boldsymbol{q}}' = [\tilde{u}', \tilde{v}', \tilde{w}', \tilde{b}', \tilde{p}']^T$. The two parts are discussed separately below.

B. Computational parameters and basic flow

The parameters for the benchmark case are $\mathrm{Ro} = \mathrm{Fr} = 0.1$, $A_R = 0.02$, $\mathrm{Re} = 10^7$, and $\mathrm{Pr} = 1$. For reference, corresponding dimensional parameters are listed in Table I if U_0^* is set to 0.3 m/s and the latitude is 16°N. These parameters are order-of-magnitude estimates from the current system in Fig. 1. Note that Ro will be varied in Sec. V for a parameter study; we keep Fr = Ro to simplify the parameter space, so $\varepsilon = \mathrm{Ro}$ holds.

As mentioned in Sec. I, we consider meridional current and undercurrent (KC-LUC), i.e., y is along-current and x is cross current. Due to the large Re, the viscous and diffusion terms are neglected for the basic flow. In the 1D-LSA problem, $\bar{V} = \bar{V}(z)$ and $\bar{U} = \bar{W} = 0$ are assumed. However, as will be shown below, the thermal-wind balance further restricts that $\bar{V}(z)$ must be a linear function $\bar{V} = z + C_2$ instead of being arbitrarily selected (C_2 is a constant), which limits the application of 1D-LSA to realistic oceanic flows. This restriction is relaxed in the framework of BIA, where the zonally nonuniform stratification resulting from a nonlinear $\bar{V}$ can be accounted for in the $x - z$ plane, so $\bar{V}$ can be an arbitrary 2D function $\bar{V}(x, z)$ subject to appropriate boundary conditions. To be specific, $\bar{\boldsymbol{q}}(x, z)$ is assumed to be $\bar{V} = \bar{V}(x, z)$, $\bar{U} = \bar{W} = 0$, $\bar{B} = \bar{B}(x, z)$, $\bar{P} = \bar{P}(x, z)$, which automatically satisfies the continuity and buoyancy equations. The other equations in Eq. (6) lead to the thermal-wind balance as $\partial\bar{V}/\partial z = \partial\bar{B}/\partial x$. Therefore, the buoyancy field for a given $\bar{V}$ is obtained as

$$\bar{B} = \int \frac{\partial \bar{V}}{\partial z}\,dx + C_z(z), \quad \frac{\partial \bar{B}}{\partial z} = \int \frac{\partial^2 \bar{V}}{\partial z^2}\,dx + \frac{dC_z(z)}{dz}, \tag{7}$$

where C_z is an arbitrary function of z. For the 1D-LSA problem, the basic-flow coefficient $\partial\bar{B}/\partial z$ is required to be independent of x, so $\partial^2\bar{V}/\partial z^2 = 0$ is enforced. In a more general setup, Wang *et al.*

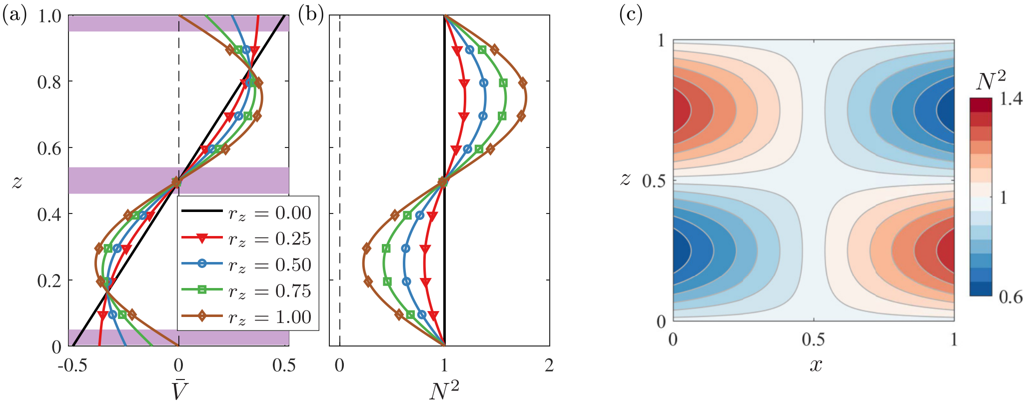

FIG. 2. One-dimensional velocity case ($r_x = 0$): Vertical distribution of the basic-flow (a) meridional velocity and (b) buoyancy frequency (at $x = 0$) with different r_z and the (c) buoyancy frequency contour in the $r_z = 0.5$ case.

[15] analyzed $\bar{V}(z)$ in the shapes of hyperbolic tangent and double jets, but artificially ignoring $\partial^2\bar{V}/\partial z^2$ could introduce additional errors. As will be shown in Sec. IV A, the above simplification indeed causes a deviation in the disturbance growth rate for the case studied. For a given $\bar{V}(x, z)$, two requirements are posed when selecting C_z in Eq. (7). The first is that the spatial average of the nondimensional, or the normalized $N^2 = N^{*2}/\bar{N}^{*2}$, needs to be 1:

$$\frac{1}{\Omega}\iint_\Omega N^2\, dxdz = \frac{1}{\Omega}\iint_\Omega \varepsilon\frac{\partial\bar{B}}{\partial z}\, dxdz = 1, \tag{8}$$

where Ω is the domain area. The second is that N^2 should be positive everywhere, ensuring hydrostatic stability. A simple linear distribution $C_z = cz$ is adopted with c determined from Eq. (8).

An idealized analytical flow is considered in this work. The domain for the cross section is $x, z \in [0, 1]$ after nondimensionalization. For ease of comparing with previous 1D-LSA results, the present analysis starts from the Eady-type 1D linear profile $\bar{V}_{\text{lin}}(z) = z - 0.5$. Afterwards, we take two steps for a more realistic description of the current-undercurrent system. First, $\bar{V}_{\text{lin}}$ is gradually transitioned to a 1D sine type. Second, an increasingly strong zonal variation of $\bar{V}$ is allowed. We will focus on three aspects in particular, namely (i) the difference between 1D-LSA and BIA results for the 1D case $\bar{V}(z)$, (ii) different types of unstable modes when the shape of $\bar{V}$ is changed, and (iii) the relative importance of horizontal and vertical shear in inducing instability.

Specific expressions of $\bar{V}$ and $\bar{B}$ are described below. First, in the 1D case $\bar{V}(z)$, the eventual sine-type velocity is designed to be $\bar{V}_{\sin} = \bar{V}_m \sin(-2\pi z)$, with the constant $\bar{V}_m$ controlling the mass flux. For smooth transition from $\bar{V}_{\text{lin}}$ to $\bar{V}_{\sin}$, we adopt a simple linear combination as

$$\bar{V}(z; r_z) = \bar{V}_{\text{1D}}(z; r_z) = (1 - r_z)\bar{V}_{\text{lin}}(z) + r_z\bar{V}_{\sin}(z), \tag{9}$$

where $r_z \in [0, 1]$ is a varying weight coefficient. For variable control, $\bar{V}_m$ is determined to be $\pi/8$, so the absolute flow flux in the upper and lower layers, $\int_0^1 |\bar{V}_{\text{1D}}|\, dz$, remains unchanged as r_z varies. For demonstration, $\bar{V}$ and N^2 with different r_z are plotted in Fig. 2. Note that it is a simplification that $\bar{V}_{\text{1D}}$ is designed to be an antisymmetric distribution about $z = 0.5$. In the $r_z > 0$ case, the vertical shear is not uniform, whose maximum rises as r_z increases. At $r_z = 0.25$, $\bar{V}$ has small gradients near two vertical boundaries, close to a free-slip flow. For the cases $r_z \geqslant 0.5$, there appear to be two high-shear regions of opposite signs of shear as that from $\bar{V}_{\text{lin}}$ near the top and surface, as labeled in the shaded area. These high-shear regions related to internal velocity peaks are more realistic for a

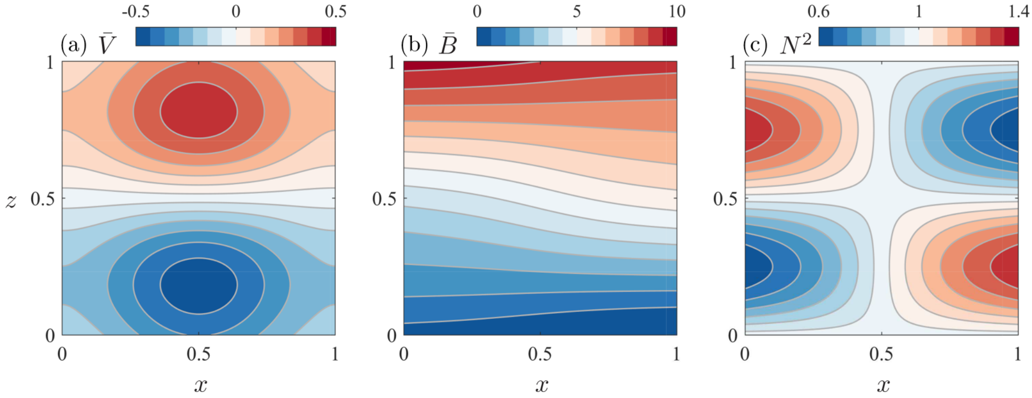

FIG. 3. Two-dimensional velocity case: Contours of the basic-flow (a) meridional velocity, (b) buoyancy, and (c) buoyancy frequency with $r_z = 0.5$, $r_x = 0.4$.

bottom boundary than for a surface one. In this sense, the latter is more artificial, so when discussing the boundary high-shear region below (in Sec. V), we are referring to the bottom boundary. Due to the nonzero $\partial^2\bar{V}/\partial z^2$ when $r_z > 0$, N^2 experiences vertical and horizontal variations. As shown in Fig. 2(c), N^2 is unity along $x = 0.5$, and exhibits an antisymmetric distribution on the two sides.

Zonal variations of $\bar{V}$ are further allowed, which is ubiquitous in realistic oceanic flows [31]. In connection with Eq. (9), the velocity is designed to be

$$\bar{V}(x, z; r_x, r_z) = \bar{V}_{1\mathrm{D}}(z; r_z)[1 + r_x \cos(2\pi x - \pi)], \tag{10}$$

where $r_x \in [0, 1]$ is also a weight coefficient. When $r_x = 0$, $\bar{V}(x, z) = \bar{V}_{1\mathrm{D}}$ and when $r_x = 1$, $\bar{V}$ diminishes to zero at $x = 0, 1$. The maximum $\bar{V}$ is at $x = 0.5$ and increases as r_x rises, but the absolute flow flux $\int_0^1\int_0^1 |\bar{V}|\, dz\, dx$ remains unchanged. The spatial distribution of $\bar{V}$, $\bar{B}$, and N^2 is plotted in Fig. 3 for the case $r_z = 0.5$ and $r_x = 0.4$. As r_x increases, the vertical shear along $x = 0.5$ is strengthened, and so is the horizontal tilting of $\bar{B}$. In contrast, the vertical shear near the two zonal boundaries diminishes.

C. Biglobal instability analysis

Contrary to 1D-LSA [Eq. (1)], no zonal Fourier decomposition is made in BIA, and the disturbance takes the form of $\tilde{\boldsymbol{q}}' = \hat{\boldsymbol{q}}'(x, z)\exp[i(-\omega t + k_y y)]$. We consider a temporal instability problem, so $\omega = \omega_r + i\omega_i$ is complex with ω_r the circular frequency and ω_i the growth rate. The governing equation for $\hat{\boldsymbol{q}}'$ is derived from $\mathcal{L}(\bar{\boldsymbol{q}} + \tilde{\boldsymbol{q}}') - \mathcal{L}(\bar{\boldsymbol{q}}) = \boldsymbol{0}$ (defined in Sec. II A). After using Eq. (2) and dropping the nonlinear terms of $\tilde{\boldsymbol{q}}'$, the homogeneous system leads to an eigenvalue problem for ω:

$$\begin{aligned}
i\mathrm{Ro}k_y\bar{V}\hat{u}' - \hat{v}' + \frac{\partial \hat{p}'}{\partial x} - \frac{\mathrm{Ro}}{\mathrm{Re}A_R^2}\frac{\partial^2 \hat{u}'}{\partial z^2} &= i\mathrm{Ro}\,\omega\hat{u}',\\
i\mathrm{Ro}k_y\bar{V}\hat{v}' + \left(\mathrm{Ro}\frac{\partial \bar{V}}{\partial x} + 1\right)\hat{u}' + \varepsilon\mathrm{Ro}\frac{\partial \bar{V}}{\partial z}\hat{w}' + ik_y\hat{p}' - \frac{\mathrm{Ro}}{\mathrm{Re}A_R^2}\frac{\partial^2 \hat{v}'}{\partial z^2} &= i\mathrm{Ro}\,\omega\hat{v}',\\
i\mathrm{Fr}^2A_R^2k_y\bar{V}\hat{w}' + \frac{\partial \hat{p}'}{\partial z} - \hat{b}' &= i\mathrm{Fr}^2A_R^2\omega\hat{w}',\\
ik_y\bar{V}\hat{b}' + \frac{\partial \bar{B}}{\partial x}\hat{u}' + N^2\hat{w}' - \frac{1}{\mathrm{RePr}A_R^2}\frac{\partial^2 \hat{b}'}{\partial z^2} &= i\omega\hat{b}',\\
\frac{\partial \hat{u}'}{\partial x} + ik_y\hat{v}' + \varepsilon\frac{\partial \hat{w}'}{\partial z} &= 0.
\end{aligned} \tag{11}$$

After numerical discretization in the x and z directions, the matrix form of Eq. (11) is $\mathcal{A}\hat{\boldsymbol{Q}}' = \omega\mathcal{H}\hat{\boldsymbol{Q}}'$, where $\hat{\boldsymbol{Q}}' = [\hat{\boldsymbol{q}}'_{1,1}, \ldots, \hat{\boldsymbol{q}}'_{i,j}, \ldots, \hat{\boldsymbol{q}}'_{N_x,N_z}]^T$ contains all the variables in the $x - z$ plane with N_x and N_z the grid numbers. The global matrices $\mathcal{A}$ and $\mathcal{H}$ are of dimensions $(5N_xN_z)^2$, which is N_x^2 times larger than the 1D-LSA counterpart. The significant rise in matrix dimensions imposes a considerable challenge on the requirements of memory and computational time. To reduce the grid numbers, spectral methods are adopted for the discretization in both directions. Since the domain is finite and the basic flow is nonperiodic, the Chebyshev collocation point method is adopted in both directions. The eigenvalue problem in Eq. (11) is solved using Matlab in combination with sparse matrix techniques. The amplitude of $\hat{\boldsymbol{q}}'$ is arbitrary for linear analysis and it is normalized by $\hat{p}$ at its peak amplitude. The solver verification is detailed in the Appendix.

Considering the large computational cost of BIA, we describe more of our practical implementations. First, we calculate all the eigenvalues for a new basic flow on a coarse grid ($N_x, N_z = 20$–40) to have an overview of the instability characteristics. Different types of unstable modes are then identified. Afterwards, N_x and N_z are increased to obtain grid-independent results for specific modes. The grid-independence study is provided in the Appendix to determine the required grid density. Basically, $N_x, N_z = 41$–61 are adequate for most cases studied, while for some cases in Sec. V, the required N_z is up to 101. Oscillating unphysical modes may appear, which can be recognized and dismissed as they cannot converge with increasing grid density [39]. The approach of growth-rate decomposition (see Sec. II E) also helps identify physical modes.

D. Viscosity effects and boundary conditions

By definition, the ICL is at $z = z_c$ where $k_y^*\bar{V}^*(z_c^*) - \omega^* = \pm f^*$. For the inviscid problem, the ICL acts as a singular point for neutral modes because the denominator of the shape function tends to zero [40]. As a result, a very large N_z is required to obtain grid-independent eigenvalues for ageostrophic modes with low growth rates [13,41]. It has long been recognized that viscosity plays a significant role near the ICL to avoid the singularity [42], no matter how small they are. Therefore, viscosity and diffusivity are taken into account for the disturbance to more easily obtain grid-independent results.

A crucial problem accompanied is the treatment of boundary conditions (BCs). We consider first the inviscid version of Eq. (11), i.e., $\nu = \kappa = 0$ ($\mathrm{Re} \to \infty$). Following previous works [11], $\hat{w}'$ is set to zero at the top and bottom boundaries (rigid-lid condition), which determines the other vertical BCs. In the viscous case, we supplement the free-slip and adiabatic BCs, i.e., $\partial\hat{u}'/\partial z = \partial\hat{v}'/\partial z = \partial\hat{b}'/\partial z = 0$, to prevent the boundaries from being sources of momentum and heat. Due to the large Re, the boundary layers can be too thin to be resolved. We follow Heifetz and Farrell [43] to add top and bottom thin layers to the basic flow, within which $\partial\bar{V}/\partial z$ smoothly drops to zero at the bottom and surface. In the $\mathrm{Re} \to \infty$ limit ($\nu \to 0$, not $\nu = 0$), the thin layers degenerate and behave like two delta functions in the basic flow. For the zonal direction, a quasiperiodic BC is adopted in the 1D velocity case [$\bar{V}(z)$] to allow direct comparisons with 1D-LSA results and possible zonal extension of the domain. We term it "quasiperiodic" because $\hat{\boldsymbol{q}}'$ cannot be exactly zonally periodic due to the nonperiodicity of N^2. Since posing only two zonal BCs are adequate to close this problem, there are different combinations. Our option here is (1) $\hat{u}'$ and $\partial\hat{u}'/\partial x$, i.e., $\hat{u}'|_{x=0} = \hat{u}'|_{x=1}$, $(\partial\hat{u}'/\partial x)|_{x=0} = (\partial\hat{u}'/\partial x)|_{x=1}$. To further justify, we have also examined other four combinations, namely (2) $\hat{p}'$, $\partial\hat{p}'/\partial x$; (3) $\hat{u}'$, $\hat{p}'$; (4) $\hat{u}'$, $\hat{b}'$; and (5) $\hat{u}'$, $\hat{v}'$. These five zonal BCs are not mathematically equivalent, but they slightly affect the results for the present cases, as shown in Fig. 4. Here the case $r_z = 1$ is selected, which has the strongest zonal variation of N^2 and hence is most affected by different zonal BCs. Two representative modes are calculated, termed the Phillips- and Charney-type modes (to be defined in Sec. III), respectively. Only a negligible difference in growth rate is observed in Fig. 4(a) for the Phillips mode. In

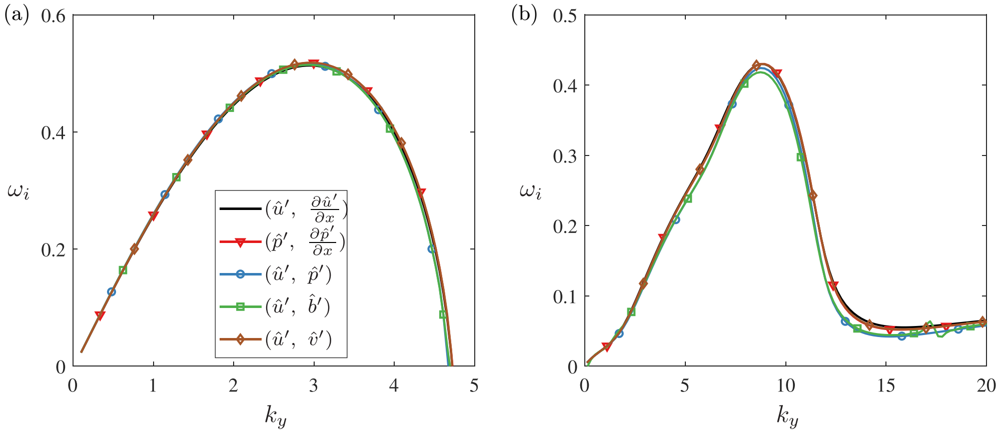

FIG. 4. Growth rates of the (a) Phillips and (b) Charney modes using different zonal BCs ($r_z = 1$, $r_x = 0$). The two variables for each case in the legend denote those of equal values at $x = 0$ and 1 as zonal BCs.

Fig. 4(b), the difference is slightly larger, but the trends are qualitatively consistent. Also, only minor differences exist in the disturbance shape functions among the five cases (not shown). Thereby, different variable combinations as zonal BCs do not alter the main conclusions in this work, and option (1) is adopted throughout. For the 2D velocity case [$\bar{V}(x, z)$], zonal BCs are less important because the maximum $\bar{V}$ is located in the middle ($x = 0.5$) and the disturbance tends to diminish towards zonal boundaries (see Sec. IV C). Option (1) is also used for consistency with the 1D velocity case.

To demonstrate the viscosity effects, the case with ageostrophic modes studied by Molemaker *et al.* [13] is examined. Figure 5 compares the normal-mode spectrums from inviscid and viscous calculations. As shown in Fig. 5(a), $|\omega_i|$ in the inviscid case keeps decreasing as N_z rises. With N_z up to 401 (Chebyshev method), the eigenvalues are still not grid independent. In fact, a maximum of over 9000 points (finite difference scheme) were used by Molemaker *et al.* [13] to obtain grid-independent unstable modes. In comparison, a series of grid-independent modes of leading ω_i are obtained with N_z of only 101 in the viscous calculation in Fig. 5(b), though the modes in

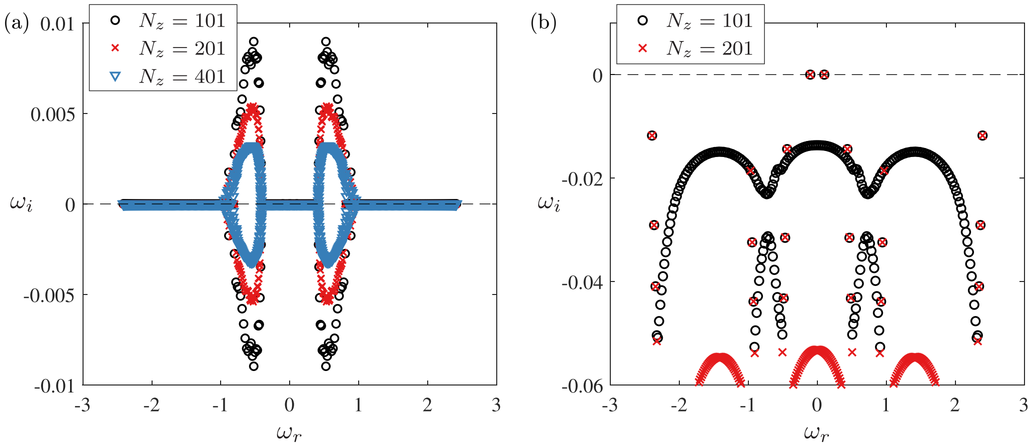

FIG. 5. Normal-mode spectrums from (a) inviscid and (b) viscous (Re = 10^6, Pr = 1) calculations using 1D-LSA with different grid numbers. The basic flow is $\bar{V}_{\text{lin}}(z)$ with $N^2 = 1$, and the case parameters are from Molemaker *et al.* [13] as Ro = Fr = $1/\sqrt{2}$, $A_R = 1$, $k_x = 0$, and $k_y = 2$ with k_x the zonal wave number as in Eq. (1).

continuous branches are still not grid independent. The above comparison highlights the significance of viscosity and diffusivity in LSA, especially when there are ICLs within the computational domain.

E. Energy budget and growth rate decomposition

Energy budget analysis can help understand instability mechanisms and identify physical modes from all the eigenmodes [19]. The total energy of the disturbance (TE, $\tilde{E}$) comprises kinetic energy (KE, $\tilde{K}$) and potential energy (PE, $\tilde{P}_E$, distinguished from the notation of pressure), whose dimensional and nondimensional forms are

$$\tilde{E}^* = \tilde{K}^* + \tilde{P}_E^*, \quad \tilde{K}^* = \frac{1}{2}(|\tilde{u}'^*|^2 + |\tilde{v}'^*|^2 + |\tilde{w}'^*|^2), \quad \tilde{P}_E^* = \frac{|\tilde{b}'^*|^2}{2N^{*2}},$$

$$2\tilde{E} = \frac{2\tilde{E}^*}{L^{*2} f^{*2}} = \mathrm{Ro}^2(\tilde{u}'^\dagger \tilde{u}' + \tilde{v}'^\dagger \tilde{v}') + \mathrm{Fr}^4 A_R^2 \tilde{w}'^\dagger \tilde{w}' + \frac{\mathrm{Fr}^2}{N^2} \tilde{b}'^\dagger \tilde{b}' \equiv \hat{\boldsymbol{q}}'^\dagger \mathbf{M}_E \hat{\boldsymbol{q}}', \tag{12}$$

where † denotes the complex conjugate and $\mathbf{M}_E$ is a diagonal positive semidefinite matrix; $\mathbf{M}_K$ and $\mathbf{M}_P$ for $\tilde{K}$ and $\tilde{P}_E$ are similarly defined, satisfying $\mathbf{M}_K + \mathbf{M}_P = \mathbf{M}_E$. Therefore, we can obtain the TE (or KE, PE) budget equation after left-multiplying $\hat{\boldsymbol{q}}'^\dagger \mathbf{M}_E$ (or $\hat{\boldsymbol{q}}'^\dagger \mathbf{M}_K$ and $\hat{\boldsymbol{q}}'^\dagger \mathbf{M}_P$) to Eq. (11) and adding the complex conjugate. Using Eq. (2), $\tilde{E}$ and its material derivative are calculated as

$$2\tilde{E} = \hat{\boldsymbol{q}}'^\dagger \mathbf{M}_E \hat{\boldsymbol{q}}' \exp(2\omega_i t) \equiv 2\hat{E} \exp(2\omega_i t), \quad \frac{D\tilde{E}}{Dt} = \frac{\partial \tilde{E}}{\partial t} + \bar{V} \frac{\partial \tilde{E}}{\partial y} = 2\omega_i \tilde{E}. \tag{13}$$

The resulting energy budget equations for $\hat{K}$, $\hat{P}_E$, and $\hat{E}$ are

$$\begin{aligned} 2\omega_i \hat{K} &= (\mathcal{P}_x + \mathcal{P}_z) + \Pi + \mathcal{C} + \mathcal{F} + \mathcal{V}, \\ 2\omega_i \hat{P}_E &= \mathcal{B}_x + \mathcal{B}_z + \mathcal{D}, \\ 2\omega_i \hat{E} &= (\mathcal{P}_x + \mathcal{P}_z) + \Pi + \mathcal{C} + \mathcal{B}_x + \mathcal{V} + \mathcal{D}. \end{aligned} \tag{14}$$

Here the work of Coriolis force is $\mathcal{C} = -\mathrm{Ro}\Re(\hat{v}'^\dagger \hat{u}' - \hat{u}'^\dagger \hat{v}') = 0$, and the expressions of other terms are

$$\begin{aligned} \text{Velocity shear production } \mathcal{P}_x &= -\mathrm{Ro}^2 \Re\left(\frac{\partial \bar{V}}{\partial x} \hat{v}'^\dagger \hat{u}'\right), \quad \mathcal{P}_z = -\varepsilon \mathrm{Ro}^2 \Re\left(\frac{\partial \bar{V}}{\partial z} \hat{v}'^\dagger \hat{w}'\right), \\ \text{Pressure work } \Pi &= -\mathrm{Ro}\Re\left(\hat{u}'^\dagger \frac{\partial \hat{p}'}{\partial x} + \hat{v}'^\dagger \frac{\partial \hat{p}'}{\partial y} + \varepsilon \hat{w}'^\dagger \frac{\partial \hat{p}'}{\partial z}\right), \\ \text{Buoyancy flux } \mathcal{F} &= \mathrm{Fr}^2 \Re(\hat{w}'^\dagger \hat{b}'), \\ \text{Buoyancy production } \mathcal{B}_x &= -\frac{\mathrm{Fr}^2}{N^2} \Re\left(\frac{\partial \bar{B}}{\partial x} \hat{b}'^\dagger \hat{u}'\right), \quad \mathcal{B}_z = -\mathrm{Fr}^2 \Re(\hat{b}'^\dagger \hat{w}') = -\mathcal{F}, \\ \text{Viscous, diffusion terms } \mathcal{V} &= \frac{\mathrm{Ro}^2}{\mathrm{Re} A_R^2} \Re\left(\hat{u}'^\dagger \frac{\partial^2 \hat{u}'}{\partial z^2} + \hat{v}'^\dagger \frac{\partial^2 \hat{v}'}{\partial z^2}\right), \mathcal{D} = \frac{\mathrm{Fr}^2}{\mathrm{RePr} A_R^2 N^2} \Re\left(\hat{b}'^\dagger \frac{\partial^2 \hat{b}'}{\partial z^2}\right), \end{aligned} \tag{15}$$

where $\Re(\cdot)$ denotes the real part of complex. As can be seen, the phases of the disturbance components are also important for energy transfers. The terms $\mathcal{P} = \mathcal{P}_x + \mathcal{P}_z$ and $\mathcal{B} = \mathcal{B}_x + \mathcal{B}_z$ contain the products of the basic-flow gradient and the disturbance, so they represent direct energy transfers between the basic flow and the disturbance. Besides, $\mathcal{P}_x$ reflects the contribution from barotropic instability through horizontal shear, so it can measure the departure from 1D-LSA (or 1D-QG-LSA) results.

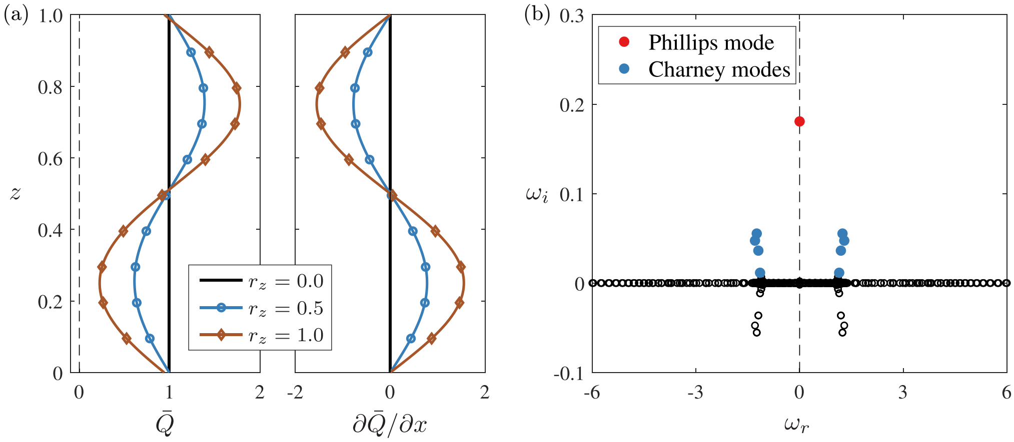

FIG. 6. (a) Vertical distribution of the basic-flow potential vorticity ($x = 0$) and its gradient with different r_z, and (b) the global mode spectrum from BIA with Ro = 0.01 and no viscosity ($k_y = 4.0$, $r_z = 0.5$).

More importantly, Eq. (14) allows a decomposition of the mode growth rate, so the contribution of each physical process to the disturbance growth can be quantified [26,44]. Taking the equation for $\hat{K}$ as an example, the decomposition is realized after a spatial integration of Eq. (14) over Ω as

$$\omega_i = \sigma_{K,\mathcal{P}_x} + \sigma_{K,\mathcal{P}_z} + \sigma_{K,\Pi} + \sigma_{K,\mathcal{F}} + \sigma_{K,\mathcal{V}}, \tag{16}$$

where, e.g., $\sigma_{K,\mathcal{P}_x}$ is the growth rate contributed by $\mathcal{P}_x$ to $\hat{K}$, computed as

$$\sigma_{K,\mathcal{P}_x} = \left(\iint_\Omega \mathcal{P}_x dxdz\right)/(2\hat{K}_{\text{int}}), \quad \hat{K}_{\text{int}} = \iint_\Omega \hat{K} dxdz. \tag{17}$$

Other terms in Eq. (16) are defined likewise. The contribution of the pressure work term is zero if the flow is geostrophic and hydrostatic. For more general flows, Gauss's theorem gives

$$\iint_\Omega \Pi dxdz = -\text{Ro}\Re\left[\oint_\Gamma (\hat{\boldsymbol{u}}'^{\dagger}\hat{p}')\cdot d\boldsymbol{S}\right], \tag{18}$$

where Γ denotes the domain boundaries and $d\boldsymbol{S}$ is the normal vector. Thereby, σ_Π is zero if the boundary condition is no penetration or periodic.

III. MODE NOMENCLATURE

The classification of unstable baroclinic modes is discussed following standard usage [18,20]. Only the 1D velocity case [$\bar{V}(z)$] is considered here and the relative contribution from barotropic instability is left for discussion in Sec. IV C. The CSP condition is employed first for an overview in the QG limit. The dimensionless Ertel potential vorticity $\bar{Q}$ is expressed using Ri as

$$\bar{Q} = \frac{\bar{Q}^*}{f^*\bar{N}^{*2}} = N^2\left(1 + \text{Ro}\frac{\partial\bar{V}}{\partial x} - \frac{1}{\text{Ri}}\right), \quad \text{Ri} = \text{Fr}^{-2}\frac{N^2}{(\partial\bar{V}/\partial z)^2}. \tag{19}$$

Figure 6(a) plots $\bar{Q}$ and its horizontal gradient for different cases. From the CSP condition, the $r_z = 0$ case supports the classic Eady-type mode, while the $r_z > 0$ cases support two types. The first is analogous to the Eady type. As the maximums of $\hat{u}'$, $\hat{v}'$, $\hat{b}'$, and $\hat{p}'$ for this mode move from vertical boundaries to the interior (shown later in Sec. IV A) subject to the nonlinear vertical shear, it is termed a Phillips-type mode hereinafter. The second is Charney-type modes which are surface or bottom amplified.

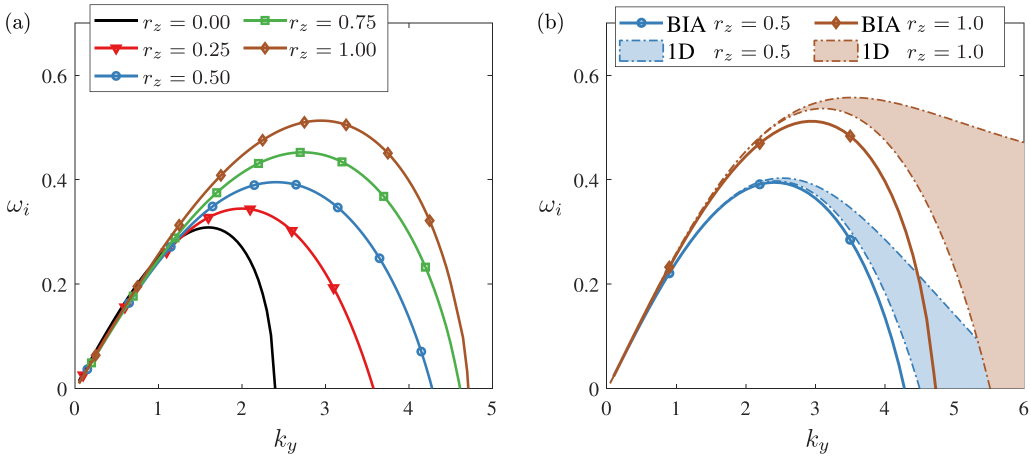

FIG. 7. Growth rates of the Phillips mode (a) from BIA and (b) from both the approximate 1D-LSA ($k_x = 0$) and BIA for varying r_z cases. For 1D-LSA, the upper and lower growth-rate envelopes are shown with $x_{\text{base}} \in [0, 1]$.

For the $r_z = 0$ case, the zero-frequency Eady mode is the only dominant one. There should be a series of Eady modes in BIA, equivalent to the modes of different k_x in 1D-LSA. Restricted by the zonal boundaries, only the discrete modes with $k_x = 2n\pi$ $(n = 0, 1, \dots)$ can exist in BIA. As the Eady mode is quickly stabilized by rising k_x, only a single unstable mode with $k_x = 0$ appears. For the $r_z > 0$ case, the Phillips-type mode has a large growth rate, as shown in Fig. 6(b). For ease of writing, the Eady mode in the $r_z = 0$ case will be regarded as a Phillips counterpart below. Besides, there exists a series of unsteady ($\omega_r \neq 0$) Charney-type modes, with no counterparts in the $r_z = 0$ case, because of the multi-high-shear-layer structure (see Fig. 2). Note that the calculation in Fig. 6(b) employs a smaller Ro = 0.01 and no viscosity temporarily only for this figure to better match the QG limit in the CSP condition. The effects of Ro and viscosity will be discussed later.

IV. PHILLIPS-TYPE MODE

A. Comparison of BIA and 1D-LSA results

The results between BIA and 1D-LSA are compared for the 1D velocity case. There are two main reasons for such comparisons. The first is to evaluate how much difference can be caused when 1D-LSA neglects the x dependence of N^2. The second is to regard the 1D-LSA results as an intermediate step, so the effects of $\bar{V}$ and N^2 variations can be distinguished. As mentioned in Sec. II B, to make 1D-LSA applicable for a nonlinear $\bar{V}(z)$, $\partial^2\bar{V}/\partial z^2$ in Eq. (7) was discarded by, e.g., Wang *et al.* [15], and then N^2 was always one irrespective of the $\bar{V}(z)$ distribution. Here we make a further approximation to 1D-LSA that vertically varying N^2 and $\bar{V}$ at an arbitrary x in Fig. 2 (denoted as x_{base}) can be used as the basic-flow for 1D-LSA. To be specific, the basic-flow coefficients in the disturbance equation are taken as $\bar{V}(z; x_{\text{base}})$, $N^2(z; x_{\text{base}})$, and $(\partial\bar{V}/\partial z)(z; x_{\text{base}})$. Local horizontal homogeneity is assumed, and the x dependence of basic-flow coefficients is dismissed. We term it "approximate 1D-LSA." In fact, the approximate 1D-LSA result is quite close to that from 1D-QG-LSA (f plane) at small Ro. Though $\bar{V}$ and N^2 of arbitrary shapes can satisfy the QG basic-flow equation, local horizontal homogeneity is also assumed for the disturbance equation.

The growth rates of the Phillips mode from BIA are displayed in Fig. 7(a) at different r_z. A clear trend is observed that with the rise of r_z, the maximum growth rate increases, and the instability regime extends to a larger k_y. The growth-rate comparison between BIA and the approximate 1D-LSA is displayed in Fig. 7(b). For the latter, we can use the basic flow at different x_{base} [same $\bar{V}(z)$

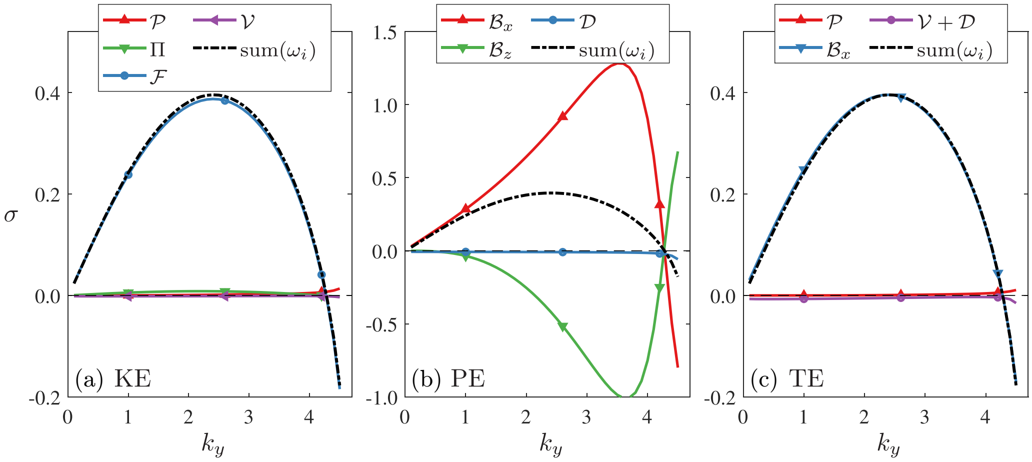

FIG. 8. Growth rate contributions of different terms to the (a) KE, (b) PE, and (c) TE of the Phillips mode ($r_z = 0.5$). The symbols in the legend are defined in Eq. (15), namely $\mathcal{P}$ (velocity shear production), Π (pressure work), $\mathcal{F}$ (buoyancy flux), $\mathcal{V}$ and $\mathcal{D}$ (viscous and diffusion terms), and $\mathcal{B}_x$ and $\mathcal{B}_z$ (buoyancy production).

but different $N^2(z)$], leading to different growth rates. Thereby, the upper and lower envelopes of the growth rates with $x_{\text{base}} \in [0, 1]$ are plotted in Fig. 7(b) for each r_z. The lower envelope is from the uniform-N^2 case ($x_{\text{base}} = 0.5$), while the upper one is from the basic flow at zonal boundaries ($x_{\text{base}} = 0, 1$). Therefore, the vertical variation of N^2 (higher average of $1/N^2$) is destabilizing with $\bar{V}$ unaltered for the present flow, consistent with the estimation from local Eady scaling that $\omega_{i,\text{Eady}} \sim 1/N$ after a vertical average. The 1D-LSA and BIA results match well in the small-k_y region. This is reasonable as seen from Eq. (11) that in the $k_y \to 0$ limit, $\hat{u}'$ and $\hat{w}'$ are both suppressed, so the terms related to $\bar{B}$ and $\bar{V}$ gradients tend to vanish. As a result, the disturbance is geostrophic and hydrostatic. However, the difference between BIA and 1D-LSA gradually increases with the rise of k_y. The mode in BIA is more stable and covers a narrower unstable range of k_y. Since the ω_i by BIA is smaller than the lower envelope of ω_i from 1D-LSA, the simplification made in the approximate 1D-LSA leads to an overestimated growth rate and an underestimated spatial length scale, especially in the short-wave range, though the maximum ω_i does not vary much. As will be shown below, the disturbance in BIA experiences a stronger zonal variation as k_y increases, while the disturbance in 1D-LSA is always zonally uniform ($k_x = 0$). Thereby, the lower growth rate in BIA is reasonable because the increase of k_x in 1D-LSA is stabilizing for the geostrophic mode. In summary, two trends are shown in Fig. 7. The increase of the overall vertical shear has a destabilizing effect on the Phillips mode, while the basic-flow horizontal inhomogeneity, resulting from the nonlinear $\bar{V}(z)$, is stabilizing. The growth-rate decomposition is utilized below to understand further the observed trends.

B. Energy budget and disturbance structure

The moderate case $r_z = 0.5$ is analyzed first, and the decomposition for KE, PE, and TE is plotted in Fig. 8. The buoyancy flux is the only dominant contributor to the disturbance KE, confirming its baroclinic nature. The pressure-work contribution is close to but not exactly zero because $\hat{p}'$ and the velocity components are not exactly zonally periodic (Sec. II D). The viscous term is negligible and the production term has a small but increasing positive contribution with the increase of k_y. For PE, the growth-rate contribution mainly comes from two buoyancy production terms; $\mathcal{B}_x$ is a huge energy source, while $\mathcal{B}_z$ is a strong energy sink, responsible for the energy transfer from PE to KE. The above describes a classic route of energy transfer in baroclinically unstable flow [4].

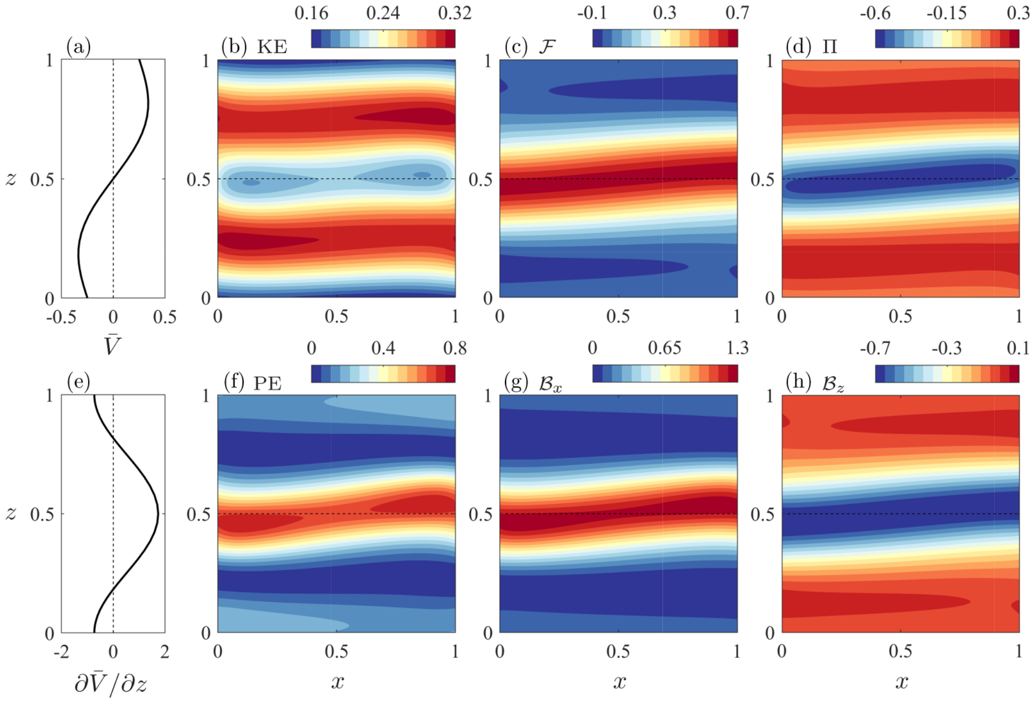

FIG. 9. Basic-flow (a) velocity and (e) its vertical gradient and [(b)–(d) and (f)–(h)] the contours of different energy-budget terms for the most unstable mode ($k_y = 2.41$) in the $r_z = 0.5$ case: (b) KE, (c) $\mathcal{F}$, (d) Π, (f) PE, (g) $\mathcal{B}_x$, and (h) $\mathcal{B}_z$. The terms are normalized by $2\hat{E}_{\text{int}}$ [see Eq. (17)], and their symbols are the same as those in Fig. 8.

The spatial structure of different energy budget terms is further investigated, focusing mainly on the most unstable mode. The KE mainly concentrates around the peak amplitude of $\bar{V}$ [Fig. 9(a)], which also holds for other cases with different r_z. In comparison, PE is restored primarily around the centerline $z = 0.5$. The maximum amplitudes of $\hat{w}'$ (shown later), $\hat{b}'$, and thus $\mathcal{F}$ are all located near $z = 0.5$, where the energy transfer from PE to KE occurs intensively. Though σ_Π is negligible, Π has a relatively large amplitude throughout the domain, so its central role is redistributing disturbance energy and hence determines the KE distribution. The spatial distribution of the two buoyancy production terms [Figs. 9(g) and 9(h)] is closely related to the gradients of $\bar{B}$. As a result, the large PE near the centerline is primarily owing to the high vertical strain there. It is worth mentioning that the spatial structure in Fig. 9 only slightly varies with k_y within the unstable range. With k_y approaching zero, KE and PE tend to be more zonally uniform, as discussed in Sec. IV A.

The growth-rate decomposition results are further compared among different cases, as shown in Fig. 10 ($r_z = 0$, 0.5, and 1). The term $\mathcal{B}_x$ is the dominant contributor to the growth rate in each case and thus responsible for the destabilizing effect. As shown in Fig. 9(e), $\mathcal{B}_x$ is primarily influenced by the vertical strain, which is related to Ri [see Eq. (19)]. Therefore, the main reason for the rise of $\sigma_{E,\mathcal{B}_x}$ as r_z increases is the stronger $|\partial\bar{V}/\partial z|$, or nondimensionally, the higher $1/\text{Ri}$. This positive correlation is consistent with the observation by Barth [25]. Meanwhile, the energy transfer from PE to KE is strengthened as r_z increases. In addition to $\mathcal{B}_x$, there are noticeable differences for other terms among different cases. In the $r_z = 0$ case, all terms except $\sigma_{E,\mathcal{B}_x}$ are zero throughout the unstable regime, associated with the zero k_x. As r_z increases, $\mathcal{P}$, $\mathcal{V}$, and $\mathcal{D}$ have increasingly large contributions to the growth rate in the short-wave regime. The rise of $\mathcal{P}$ indicates a more substantial energy transfer to ageostrophic motions in the small-scale range. Furthermore, as $\mathcal{P}$ and $\mathcal{V}$ are both

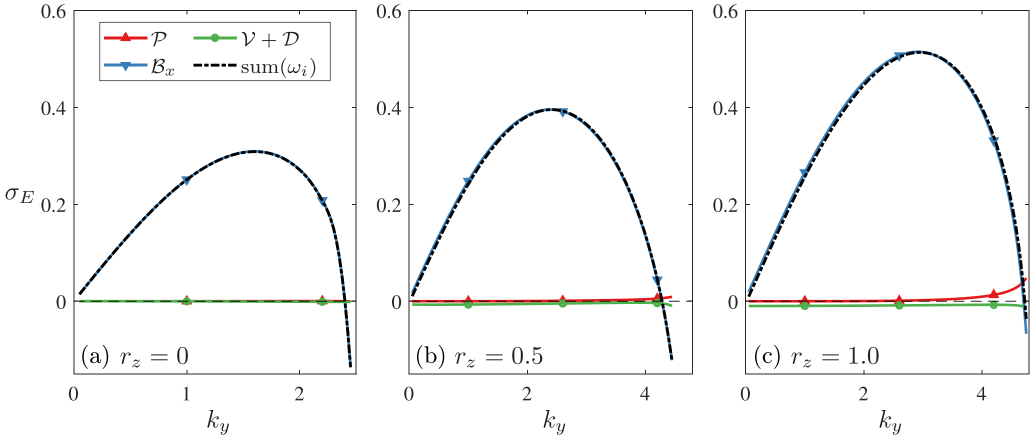

FIG. 10. Growth rate contributions of different terms to the TE of the Phillips mode in the cases (*a*) $r_z = 0$, (*b*) $r_z = 0.5$, and (*c*) $r_z = 1.0$. See Fig. 8 for the term symbols.

proportional to Ro, their increase indicates a more severe loss of geostrophic balance suggested by Molemaker *et al.* [13].

In summary, the strong vertical shear between the current and undercurrent supports the Phillips-type mode of a high growth rate. The mode is destabilized with a stronger vertical shear and thus smaller Ri. Meanwhile, ageostrophic motions are strengthened in the short-wave range at higher r_z. If using 1D-LSA (and also 1D-QG-LSA), then the growth rate and the unstable k_y range of this mode can be overestimated in the short-wave region, though the maximum growth rate does not vary much. Therefore, BIA is important for analyzing the flow of nonuniform vertical shear and strong zonal inhomogeneity.

C. Contribution of horizontal shear

The 2D velocity case [$\bar{V}(x, z)$ in Eq. (10)] is considered here. The moderate case $r_z = 0.5$ is adopted throughout this subsection, to be consistent with Sec. IV B. By conducting BIA, the zero-frequency mode, analogous to the Phillips mode in Sec. IV A, still has a high growth rate, as shown in Fig. 11 for different r_x cases. The special focus here is on the relative contributions of vertical and

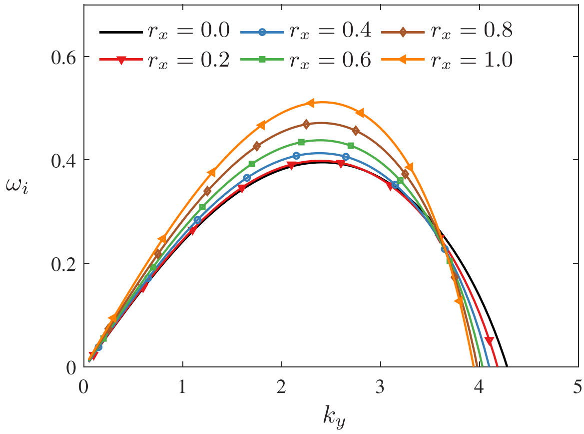

FIG. 11. Growth rate of the Phillips mode with different meridional wave numbers in different r_x cases.

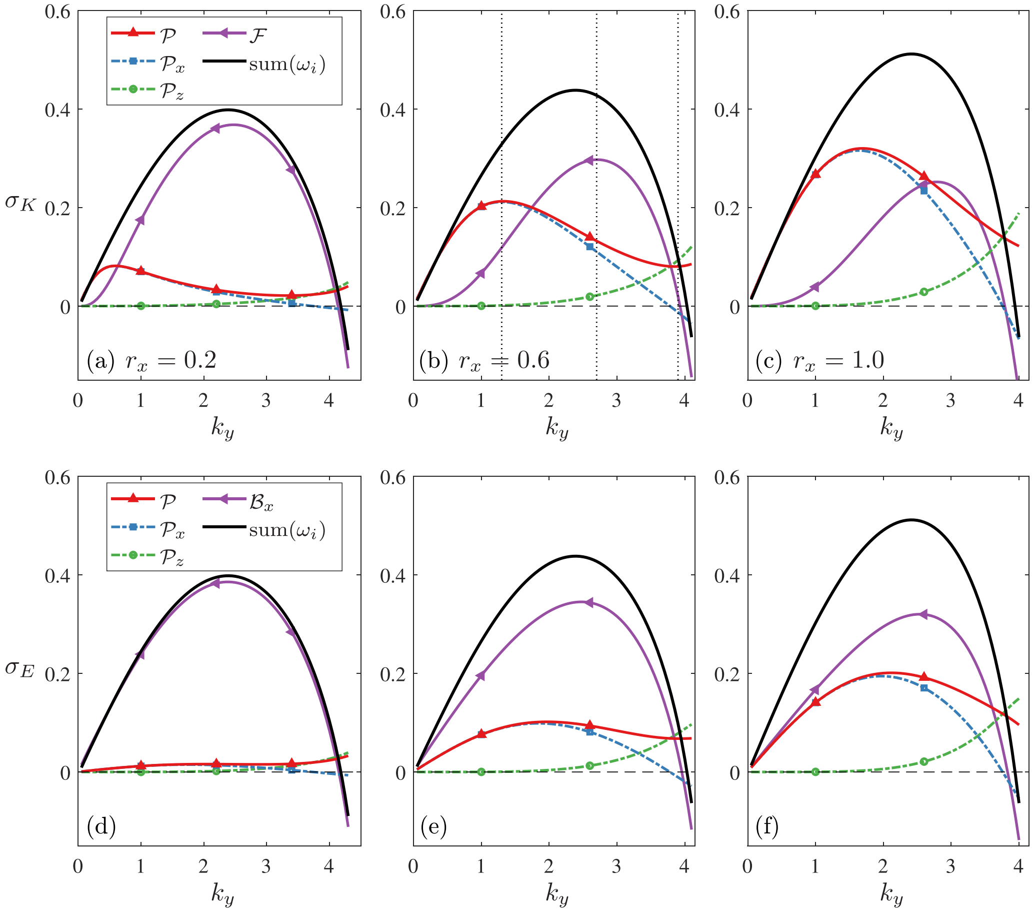

FIG. 12. Growth rate contributions of different terms to the [(a)–(c)] KE and [(d)–(f)] TE of the unstable mode in the cases [(a) and (d)] $r_x = 0.2$, [(b) and (e)] $r_x = 0.6$, and [(c) and (f)] $r_x = 1.0$. See Fig. 8 and Eq. (15) for the term symbols.

horizontal shear, so the 1D-LSA results are not provided. Compared with Fig. 7(a), the growth-rate variation of the unstable mode with r_x is much milder than that with r_z. Meanwhile, the short-wave cutoff becomes smaller, and no long-wave cutoff is present for all cases. Smith [45] also remarked that the mesoscale zonally nonuniform flow induced higher eddy amplitudes than the uniform one using a QG model, where the beta effect was the main origin.

The growth-rate decomposition is performed to identify the responsible physical term for destabilization. The evolution of the contributing components to PE bears a strong resemblance to the 1D velocity case [see Fig. 8(b)] and thus is not shown here. The decomposition results for KE, however, exhibit distinct features, as shown in Fig. 12. The pressure work and viscous terms are not displayed due to their negligible contributions. As one rises r_x, $\mathcal{P}$ has an increasingly large contribution to the growth rate and surpasses that of the buoyancy flux when $r_x = 1$. The two components of $\mathcal{P}$, namely $\mathcal{P}_x$ and $\mathcal{P}_z$, are both strengthened with the rise of r_x, though their active k_y ranges are rather different. Therefore, the growth of KE is not dominated by the buoyancy flux alone (not mostly transferred from PE). Instead, mean velocity gradients, including both horizontal and vertical shear, have direct contributions. As $\mathcal{P}$ is proportional to Ro, the unstable mode in Fig. 12 is not pure geostrophic but is a mixed barotropic and baroclinic type. Regarding KE, the long-wave range is more barotropic-like, while the short-wave range is more baroclinic-like. Figures 12(d)–12(f)

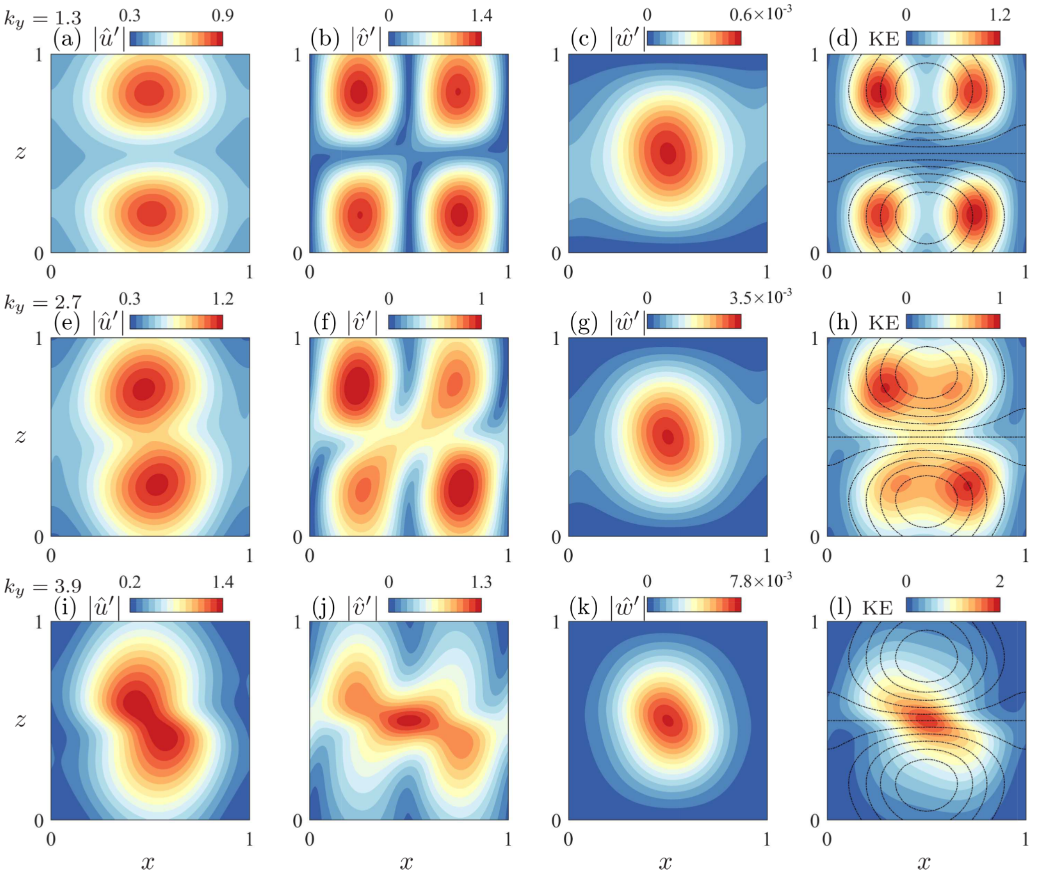

FIG. 13. Contours of the velocity components and KE of the modes at [(a)–(d)] $k_y = 1.3$, [(e)–(h)] $k_y = 2.7$, and [(i)–(l)] $k_y = 3.9$ in the $r_x = 0.6$ case: [(a), (e), and (i)] zonal velocity, [(b), (f), and (j)] meridional velocity, [(c), (g), (k)] vertical velocity, and [(d), (h), and (l)] KE. The black dashed lines in [(d), (h), and (l)] are the contours of $\bar{V}$ (uniform levels hereinafter).

show the growth-rate decomposition for TE, where $\sigma_{\mathcal{P}}$ is lower compared to that for KE since the denominator increases from $\hat{K}$ to $\hat{E}$ [see Eq. (17)]. As a result, $\sigma_{\mathcal{P}}$ is basically lower than $\sigma_{\mathcal{B}_x}$ within the unstable regime. It is also conjectured that at a higher Ro, $\mathcal{P}$ will occupy a more significant portion in supporting the mode growth. The above observation highlights the significance of using BIA for realistic oceanic flows, in which way the coupling effects of different mechanisms can be considered and the relative importance of different instabilities can be quantitatively distinguished.

The spatial structures of $\mathcal{P}_x$ and $\mathcal{P}_z$ are further discussed. From Fig. 12, $\mathcal{P}_x$ is more active at small k_y, while $\mathcal{P}_z$ has high amplitudes at large k_y. Therefore, three representative $k_y = 1.3$, 2.7, and 3.9 are selected, as labeled in Fig. 12(b). The three velocity components and KE are depicted in Fig. 13, where noticeable differences among these modes are observed. For the $k_y = 1.3$ mode, the velocities and KE are nearly symmetric relative to $z = 0.5$. From the meridional momentum equation [see Eq. (11)], $\hat{v}'$ is directly influenced by $\partial\bar{V}/\partial x$. Owing to the large contribution of $\mathcal{P}_x$, $\hat{v}'$ and KE are mainly located where the horizontal shear is the strongest. In comparison, $|\hat{u}'|$ clusters around $x = 0.5$, same as $\bar{V}$. This spatial correlation of linearly growing $\hat{u}'$ and $\hat{v}'$ with the basic flow is also noted by McWilliams *et al.* [24] for a frontally unstable flow. With the increase of k_y, the velocity contours are somewhat rotated anticlockwise with the peak locations moving toward the domain center. This tendency is attributed to the increase of both $\mathcal{F}$ and $\mathcal{P}_z$ (see Fig. 12) and is further explained below. The domain center has the strongest vertical shear, so, intuitively, it is where $\mathcal{P}_z$ is the most active. Meanwhile, $\partial\bar{B}/\partial\bar{x}$ is also in high amplitude around the center and so are the buoyancy production terms and the buoyancy flux. When $k_y = 3.9$, the peak locations of $\hat{v}'$ and KE shift to the domain center. As a side effect of this movement, $\mathcal{P}_x$ diminishes because the peak locations of $\partial\bar{V}/\partial x$ and $\hat{v}'$ do not coincide, and the other way around, $\mathcal{P}_z$ increases. Compared with other velocity components, $\hat{w}'$ is least affected by k_y, located around the center for all the modes here.

In summary, when the mode is more of a barotropic type ($k_y = 1.3$ here), the disturbance KE mainly concentrates around the region of strong horizontal shear. On the contrary, when the mode is more of a baroclinic type ($k_y = 3.9$), the KE is mainly induced where the vertical shear and hence the horizontal buoyancy gradient are of large amplitudes. Furthermore, an implication is that the basic flow of the current-undercurrent system needs to be accurately resolved in both horizontal and vertical directions in order to predict better the disturbance behavior in a realistic configuration.

V. CHARNEY-TYPE MODE

As discussed in Sec. III, high-shear layers near the vertical boundary can also support geostrophic modes, distinguished from the Phillips type. For example, Roullet *et al.* [46] obtained the linear instability features of surface-amplified Charney modes by temporally solving the perturbation equation. Meanwhile, bottom-amplified Charney modes were reported to exist widely in global oceans [18]. Here BIA is utilized to reveal the features of the Charney-type modes over a wide parameter space.

A. Basic features

We start again from the 1D velocity case. The $r_z = 1$ case has the strongest vertical shear near the boundary, so this case is studied first. Figure 14(a) provides the global mode spectrum at $k_y = 4.5$. Note that Ro is decreased to 0.01, and the calculation is inviscid here to better demonstrate the modes' geostrophic nature. The effects of Ro and viscosity will be discussed in Sec. V B. As can be seen, there are a series of unsteady unstable modes in addition to the steady Phillips mode. Meanwhile, the modes appear in pairs with opposite ω_r, representing the modes near the upper and lower vertical boundaries, respectively. The contours in Figs. 14(d)–14(i) are for the modes of negative ω_r, and those of positive ω_r are located near the upper boundary in an antisymmetric style about $z = 0.5$. As discussed in Sec. II B, the bottom-amplified mode is more realistic than the surface-amplified one for the present flow, so we mainly focus on the former. The results of growth-rate decomposition manifest that over 99 % (hence not shown here) of KE (and TE) of these unsteady modes is contributed by $\mathcal{F}$ (and $\mathcal{B}_x$), indicating their geostrophic nature. The three most unstable bottom-amplified Charney modes are termed Cb-1, Cb-2, and Cb-3 modes, respectively, in a descending order of growth rate. Their growth rates and phase velocities with different k_y are displayed in Figs. 14(b) and 14(c). The Cb-1 mode has a rather high growth rate, which is comparable to the Phillips mode. This is reasonable because the vertical shear at $z = 0$ is as strong as that at $z = 0.5$ in this case [Fig. 14(j)]. Meanwhile, the unstable regime of the Cb-1 mode covers an extremely wide range of k_y, with k_y at the short-wave cutoff reaching approximately 24. Therefore, the Charney mode can play a more crucial role in inducing small-scale motions, as also noted by Roullet *et al.* [46] and Capet *et al.* [47]. From their spatial distribution, it is recognized that different Charney modes represent the structures of different zonal wave numbers $k_{x,\mathrm{Cb}} = 4n\pi$ ($n = 0, 1, \ldots$), though there is no strict zonal periodicity due to the x dependence of N^2. Furthermore, the growth rate variations of different Charney modes are consistent with the Phillips mode in that the maximum growth rate and the unstable range of k_y gradually decrease as $k_{x,\mathrm{Cb}}$ increases. Besides, the Charney mode has an increasing phase velocity $c_r = \omega_r/k_y$ with the rise of k_y, whose range is comparable to $\bar{V}$.

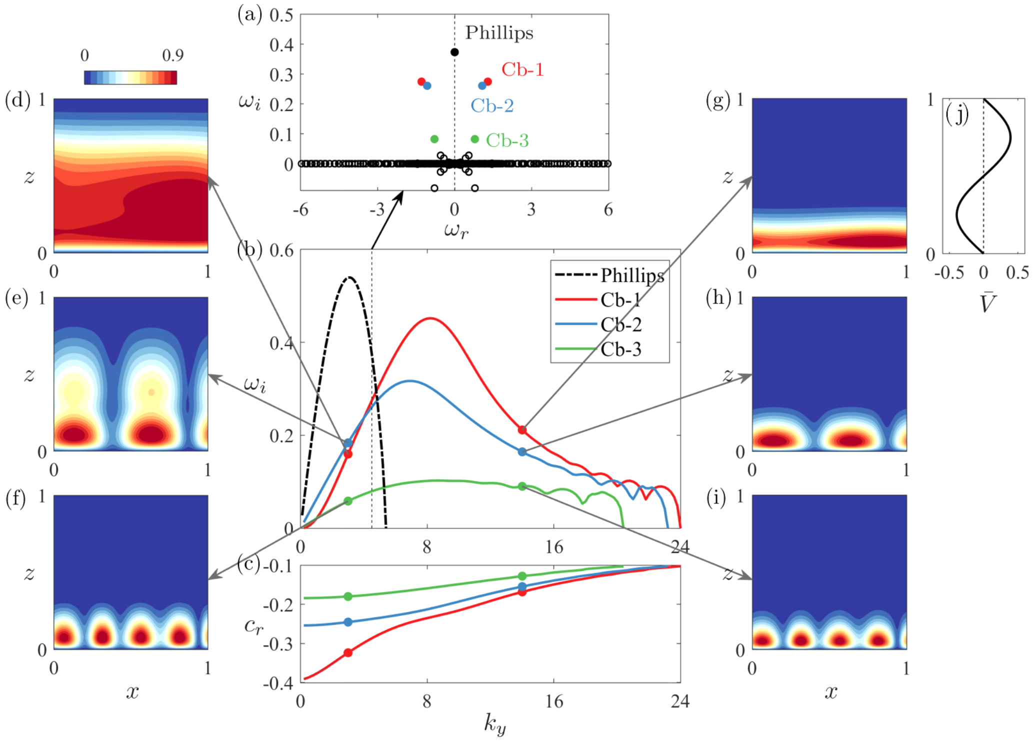

FIG. 14. (a) Global mode spectrum at $k_y = 4.5$, and the (b) growth rates, (c) phase velocities, and [(d)–(i)] contours of the normalized vertical velocity ($|\hat{w}'|/\max(|\hat{w}'|)$) for different Charney modes (inviscid, $\mathrm{Ro} = 0.01$, $r_z = 1$, $r_x = 0$). [(d) and (g)] For mode Cb-1, [(e)–(h)] for Cb-2, and [(f)–(i)] for Cb-3. $\bar{V}(z)$ is shown in (j) for reference.

For the long-wave Cb-1 and Cb-2 modes [e.g., the $k_y = 3$ modes in Figs. 14(d) and 14(e)], $\hat{w}'$ can occupy a large portion of the whole domain, though the maximum is located near the lower boundary. As k_y rises, the Charney modes are continuously compressed towards the bottom boundary. The presence of a vertical boundary severely affects the behavior of the Charney mode. For example, the maximum $\hat{w}'$ of the Phillips mode is located where the vertical shear is the strongest (see Fig. 13). However, this correlation is destroyed by the enforced BC of $\hat{w}' = 0$ at $z = 0$, leading to a large vertical gradient of $\hat{w}'$. From the disturbance continuity equation, large gradients of $\hat{u}'$ and $\hat{v}'$ are required to balance $\partial\hat{w}'/\partial z$. The horizontal distribution of the Cb-1 mode is rather uniform, i.e., $\partial\hat{u}'/\partial x$ is small, so high amplitudes of $\hat{v}'$ and k_y are needed. This can partially explain its extremely wide unstable range of k_y. Moreover, the confined spatial distribution leads to a reduction effect in the aspect ratio, which also tends to enlarge the unstable range of k_y [11,13].

B. Parameter study and viscosity effects

The effects of Ro and viscosity are investigated, which is important to make the results applicable to a wider range of realistic flows. Figure 15(a) plots the growth rates of the Cb-1 mode for varying Ro and r_z. As r_z decreases from 1 to 0.5, the Cb-1 mode is largely stabilized because of the weakening of boundary vertical shear [Figs. 16(e) and 16(j)]. The Charney mode is damped with r_z further down to 0.25. Thereby, the Charney mode is more sensitive to r_z than the Phillips mode subject to the designed velocity distribution. The increase of Ro does not decrease the maximum growth rate of the Cb-1 mode much but is severely stabilizing in the short-wave region. Similarly, the top and bottom boundary layers due to viscosity and diffusivity strongly influence the short-wave

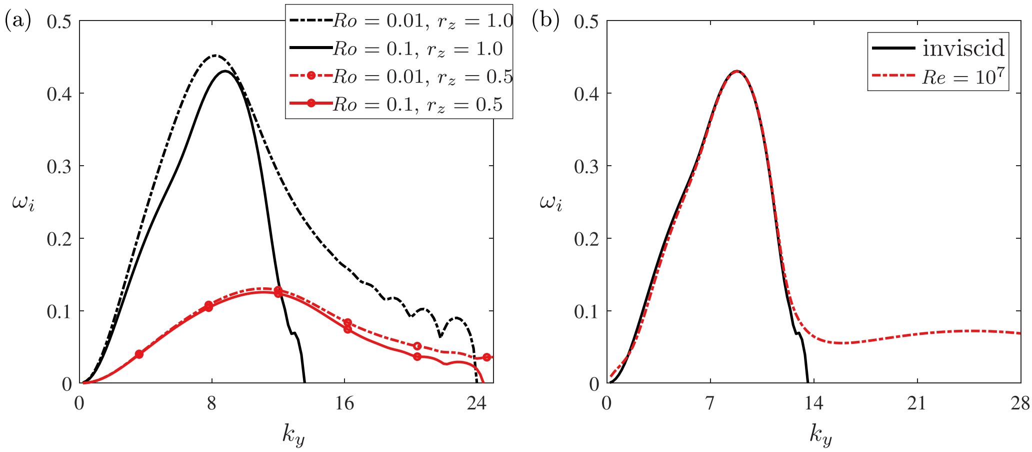

FIG. 15. Growth rates of the Cb-1 mode in the cases (a) with different Ro (Fr = Ro holds) and r_z (inviscid) and (b) with and without viscosity (Ro = 0.1, $r_z = 1$).

region, as shown in Fig. 15(b). They appear to be destabilizing, sustaining the modal growth at $k_y > 14$. These stabilizing and destabilizing effects will be explained later through the growth-rate decomposition.

The KE and PE of the most unstable Cb-1 mode are depicted in Fig. 16 for the four cases in Fig. 15(a). The peak amplitudes of KE and PE are all located at the vertical boundary with the strongest vertical shear, consistent with that in high-resolution simulations [48]. A clear trend is observed that as Ro and r_z rise, the disturbance components gradually lose zonal uniformness and the peaks move to a larger x, owing to the stronger horizontal variation of N^2. From Eq. (8), N^2 can be expressed as $N^2 = 1 + \varepsilon \int \partial^2\bar{V}/\partial z^2\, dx$, so $\partial N^2/\partial x$ is positively correlated with Ro since $\varepsilon = \mathrm{Ro}$ holds.

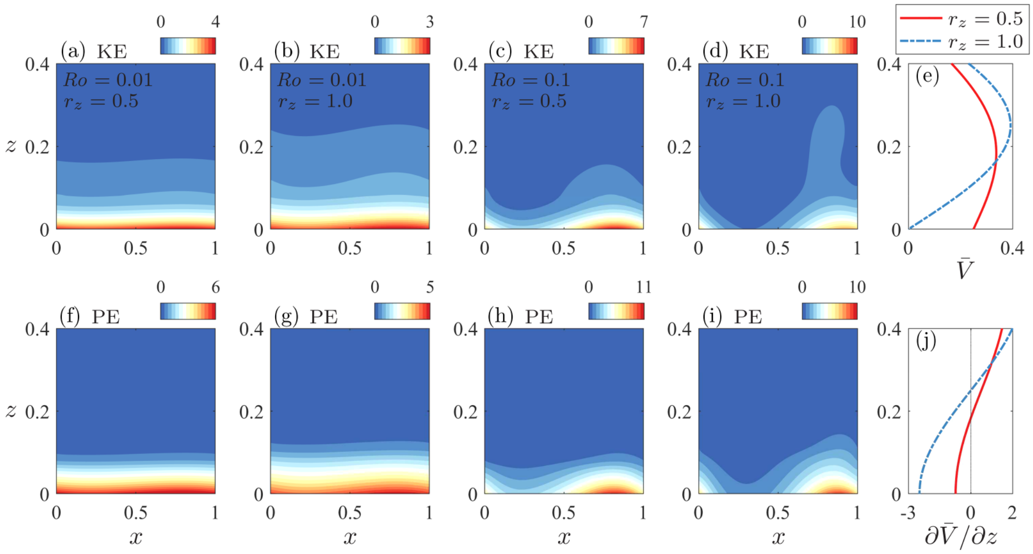

FIG. 16. Contours of [(a)–(d)] KE and [(f)–(i)] PE for the most unstable Cb-1 mode in the cases [(a) and (f)] Ro = 0.01, $r_z = 0.5$; [(b) and (g)] Ro = 0.01, $r_z = 1.0$; [(c) and (h)] Ro = 0.1, $r_z = 0.5$; and [(d) and (i)] Ro = 0.1, $r_z = 1.0$. The vertical direction is stretched for better illustration. Panels (e) and (j) give the basic-flow velocity and its gradient for reference.

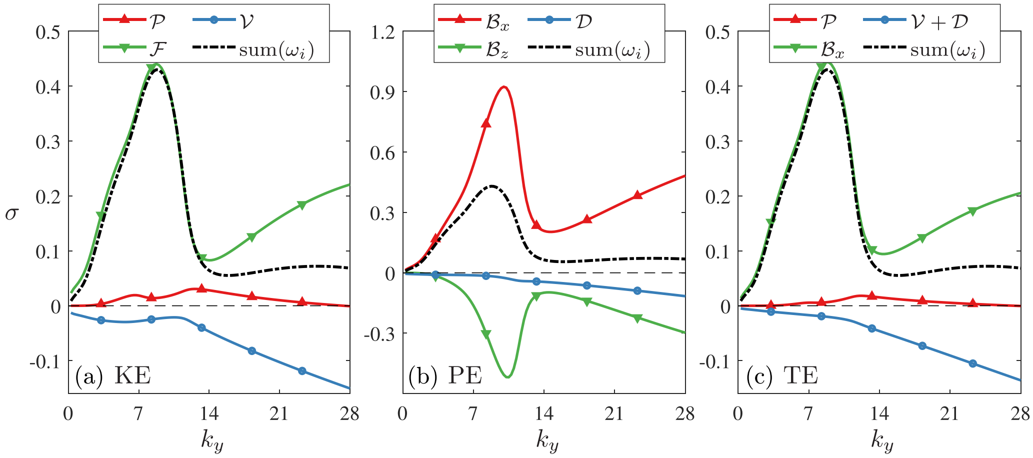

FIG. 17. Growth-rate contributions of different terms to (a) KE, (b) PE, and (c) TE for the Cb-1 mode in the benchmark case $r_z = 1$. The term symbols in the legend are the same as those in Fig. 8.

The growth-rate decomposition is employed to quantify different terms in Fig. 15. The benchmark case (Ro $= 0.1$, Re $= 10^7$) with $r_z = 1$ is selected, and the decomposition is shown in Fig. 17. The terms $\mathcal{F}$, $\mathcal{B}_x$, and $\mathcal{B}_z$ are the dominating ones for KE and PE at $k_y < 12$, so it is the increase of Fr, i.e., weaker stratification, that is mainly responsible for the stabilizing effect in Fig. 16(a) rather than the Ro increase. The terms $\mathcal{V}$ and $\mathcal{D}$ always contribute negatively to the growth rate, which is guaranteed by the free-slip and adiabatic BCs at the surface and bottom (see, e.g., Ref. [38] for proof). Nevertheless, the short waves in the viscous case remain unstable at $k_y > 14$ and exhibit higher growth rates than the inviscid case, which demonstrates the crucial differences between $\nu \to 0$ and $\nu = 0$. As shown in Fig. 14, the mode is more compressed towards the vertical boundary (confined in smaller regions) with the increase of k_y, so the inviscid short waves are stable due to the diminishing $\partial \bar{Q}/\partial x$ near the boundaries (see Fig. 6). In the viscous case, however, the locally diminishing potential vorticity gradient is counteracted by the intense vertical transport within the boundary layer, which support the mild disturbance growth. Nonetheless, the present result at very high k_y may not apply, since the small-scale motions can have complex interactions with boundary processes not modelled in this work, such as the Ekman layer and surface turbulence.

Compared with Fig. 10, ageostrophic components play more essential roles in the growth of the Charney mode, primarily due to the boundary constraint and enlarged instability regime extending into the smaller-scale region. Consequently, the Charney mode is crucial in inducing submesoscale motions and transferring interscale energy. It is also suggested that viscosity, diffusivity, and thus boundary layers need to be included to accurately resolve the small-scale Charney modes.

C. Two-dimensional velocity case

The Charney modes also exist when $\bar{V}$ is horizontally varied. Figure 18 provides an overview in the case $r_z = r_x = 1$, which has the strongest vertical and horizontal shear. As in Sec. V A, the three most unstable Charney modes are displayed. The basic characteristics of the growth rate and phase velocity curves are quite similar to those in Fig. 14. A prominent feature is that the Cb-1 mode covers a wider unstable range of k_y, and its maximum growth rate even surpasses that of the Phillips mode. Meanwhile, $\hat{w}'$ of the Charney modes concentrates mainly around the centerline $x = 0.5$ where $\bar{V}$ peaks. As k_y increases, the disturbance is more confined in the small region near $x = 0.5$ and $z = 1$. Seen from Figs. 18(f)–18(h), the Cb-1 to Cb-3 modes have one to three $|\hat{w}'|$ peaks, respectively, in analogy to the modes of different $k_{x,\mathrm{Cb}}$ in Fig. 14.

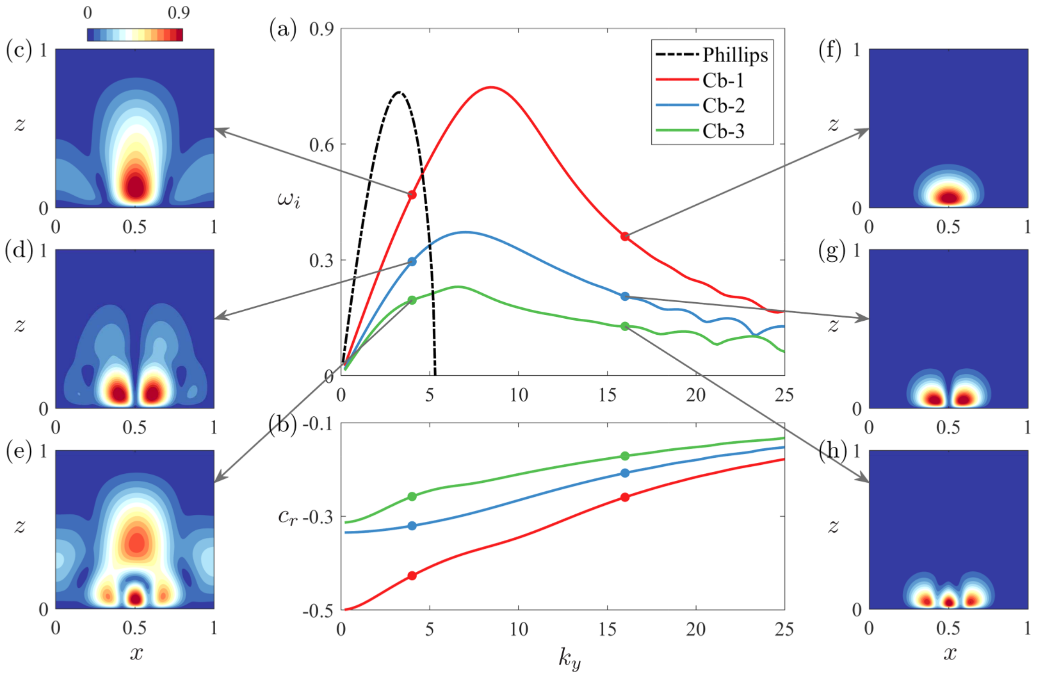

FIG. 18. (a) Growth rates and (b) phase velocities at different k_y, and [(c)–(h)] contours of the normalized vertical velocity $[|\hat{w}'|/\max(|\hat{w}'|)]$ for different Charney modes ($\omega_r < 0$) in the inviscid case (Ro $= 0.01$, $r_z = r_x = 1$). [(c) and (f)] For mode Cb-1, [(d) and (g)] for mode Cb-2, and [(e) and (h)] for mode Cb-3.

Similarly to Fig. 16, the shape functions of the most unstable Cb-1 mode are depicted in Fig. 19 for different Ro. The maximums of $\hat{p}'$, KE, and PE are all located at the vertical boundary as in Fig. 16. From the $\bar{V}$ contours in Fig. 19(c), the horizontal shear is relatively weak around $x = 0.5$

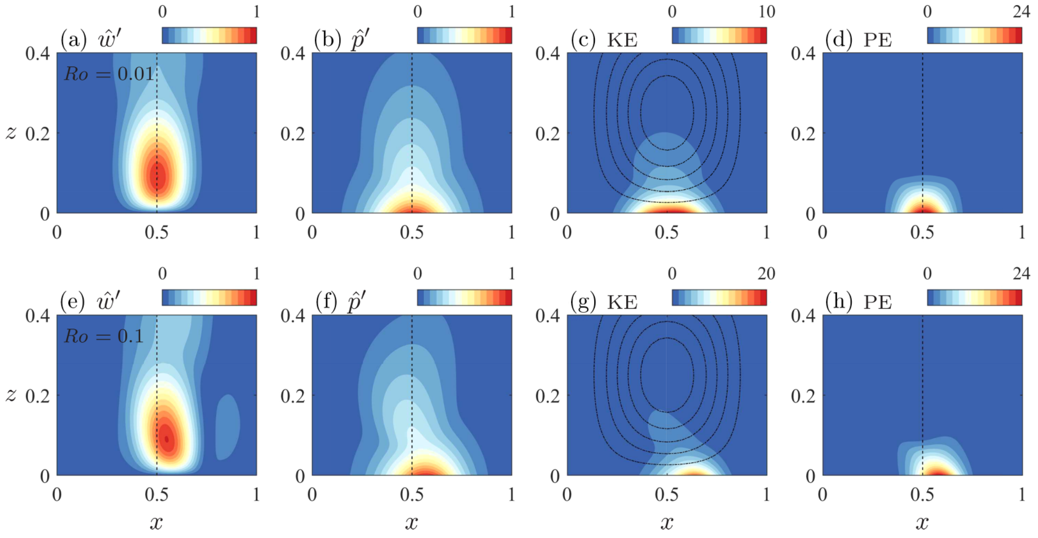

FIG. 19. Contours of [(a) and (e)] vertical velocity, [(b) and (f)] pressure, [(c) and (g)] KE, and [(d) and (h)] PE for the most unstable Cb-1 mode in the case [(a)–(d)] Ro $= 0.01$ and [(e)–(h)] Ro $= 0.1$ ($r_z = r_x = 1$). The vertical direction is stretched for better illustration. The black dashed lines in (c) and (g) are the contours of $\bar{V}$.

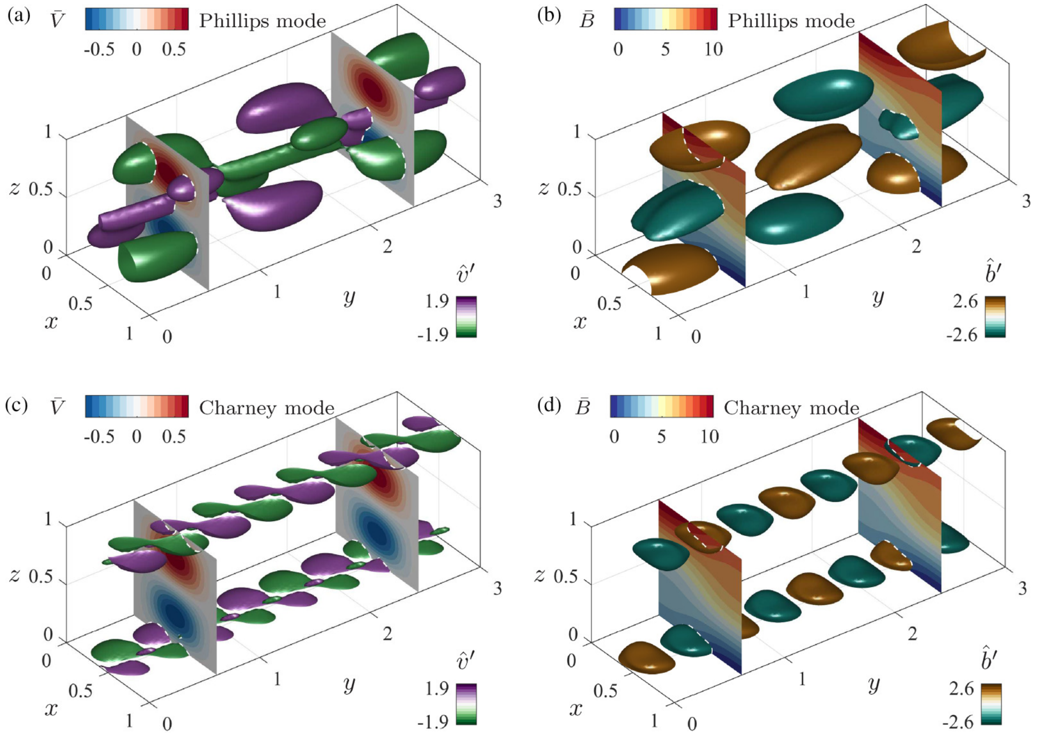

FIG. 20. Isosurfaces of the disturbance [(a) and (c)] meridional velocity and [(b) and (d)] buoyancy for the most unstable [(a) and (b)] Phillips ($k_y = 2.74$) and [(c) and (d)] Cb-1 mode ($k_y = 8.32$) in the $r_z = r_x = 1$ case. The contours on y cross sections are the basic flow. The white dashed lines are the intersection of the isosurfaces and plane contours.

where the Charney mode is active, so its contribution to the growth rate is small, different from the Phillips mode. Therefore, the primary influence of the horizontal variation of $\bar{V}$ on the Charney mode is the concentration of spatial distribution to high-vertical-shear regions. As Ro increases, the peaks of KE and PE are shifted towards a higher x, the same as in Fig. 16. Besides, the growth rate decomposition is analyzed among different cases, which strongly resembles those in Fig. 17 (hence not shown). The horizontal shear ($\mathcal{P}_x$) mainly affects the long-wave region, but its overall contribution is rather small because the horizontal shear is weak around the velocity maximum at $x = 0.5$. As in Sec. V B, the surface and bottom boundary layers destabilize the short wave and sustains the modal growth at $k_y > 15$.

Finally, Fig. 20 provides a 3D view ($\tilde{q}'$) of the Phillips and Cb-1 modes above. Note that for the Cb-1 mode, the shape functions of the two modes with $\pm\omega_r$ are combined to provide a full picture. The staggered pattern of the Phillips and the Charney modes is demonstrated. More importantly, the differences between the two modes are more easily seen, especially the different active areas and meridional wave numbers. It is worth mentioning that the Phillips and Charney modes can act simultaneously, but their potential interaction cannot be revealed in the framework of the linear analysis and awaits nonlinear analysis for a deeper understanding.

VI. SUMMARY

In this work, baroclinic instability of a current-undercurrent system, where the water in the upper and lower layers flows in opposite directions, is analyzed using the BIA. The flow parameters selected are order-of-magnitude estimates from the Western North Pacific circulation system.

Compared with the prevailing 1D-LSA, BIA can deal with the basic flow with nonuniform vertical shear and strong zonal variations. As a result, the overall instability characteristics within flow cross sections are analyzed. The Phillips-type geostrophic mode with a high growth rate is identified, primarily due to the high vertical shear between the current and undercurrent. The high-shear regions near vertical boundaries also support a series of Charney-type modes. Furthermore, the increasingly important role of ageostrophic motions is demonstrated.

For the Phillips mode, a growth-rate decomposition confirms the classic route of energy transfer for baroclinic instability. When the linear $\bar{V}(z)$ is transitioned to a sine type with high vertical shear in the middle and near vertical boundaries [at an increasing r_z, see Eq. (9)], the Phillips mode is destabilized and covers a wide unstable range of k_y because of the stronger vertical shear and thus smaller Ri. Comparisons with the 1D-LSA (and also f plane 1D-QG-LSA) results show that dismissing the horizontal basic-flow inhomogeneity, resulting from the nonlinear $\bar{V}(z)$, can lead to an overestimated growth rate and unstable range of k_y, though the maximum growth rate does not vary much. For the 2D velocity profile $\bar{V}(x, z)$, the maximum growth rate continues to increase with the rise of r_x, i.e., larger $\bar{V}$ in the middle and diminishing $\bar{V}$ towards zonal boundaries [see Eq. (10)]. Meanwhile, the zonal production term is the most significant contributor to KE in the long-wave regime, reflecting the contribution from barotropic instability. In comparison, 1D-LSA can only deal with the shear in one direction, so it cannot quantify the relative importance of baroclinic and barotropic instabilities. The unstable mode is more of a barotropic type in the long-wave range, with KE concentrating around the region of strong horizontal shear. On the contrary, the mode is more of a baroclinic type in the short-wave range, and the KE is mainly induced where the vertical shear and hence the horizontal buoyancy gradient are of large amplitudes.

In addition, a series of Charney modes are identified in the small confined region near two vertical boundaries. The most unstable bottom-amplified one, termed Cb-1 mode, is approximately zonally uniform at small Ro in the 1D velocity case. This mode can reach a comparative growth rate to the Phillips mode, and its unstable range of k_y is significantly wider, extending deep into the small-scale region. Meanwhile, ageostrophic components, including the shear production and viscous and diffusion terms, are more active in the short-wave region. The top and bottom boundary layers due to viscosity and diffusivity appear to be destabilizing for short waves and sustain the modal growth at $k_y > 14$. With an increasing horizontal variation of $\bar{V}$, the Charney mode is more destabilized because of the stronger vertical shear near $x = 0.5$, while the horizontal shear has little influence. Parameter studies are also conducted on the effects of Ro, Fr, and velocity shapes.

The present work demonstrates the advantages of employing BIA for complex flow systems, in obtaining an overall picture of different types of modes, acquiring accurate growth rates and resolving the disturbance structure subject to coupling geostrophic and ageostrophic mechanisms. In addition, the present results demonstrate the significance of accurately resolving the basic flow both vertically and horizontally in order to predict reasonably the disturbance behavior in the current-undercurrent system. Ongoing and future works are the BIA on the mean flow extracted from actual observations and simulations, as well as the nonlinear instability analysis when the disturbance is of finite amplitude.

ACKNOWLEDGMENT

This research was supported by the Key Research Project of the National Natural Science Foundation of China (41930539) and the Center for Ocean Research in Hong Kong and Macau (CORE), a joint research center between QNLM and HKUST.

APPENDIX: SOLVER VERIFICATION AND GRID-INDEPENDENCE STUDY

The 1D-LSA solver is verified first using an Eady-type case from a recent work [41]. The following nondimensional parameters are under their definition, and the basic flow is $\bar{U} = z$,

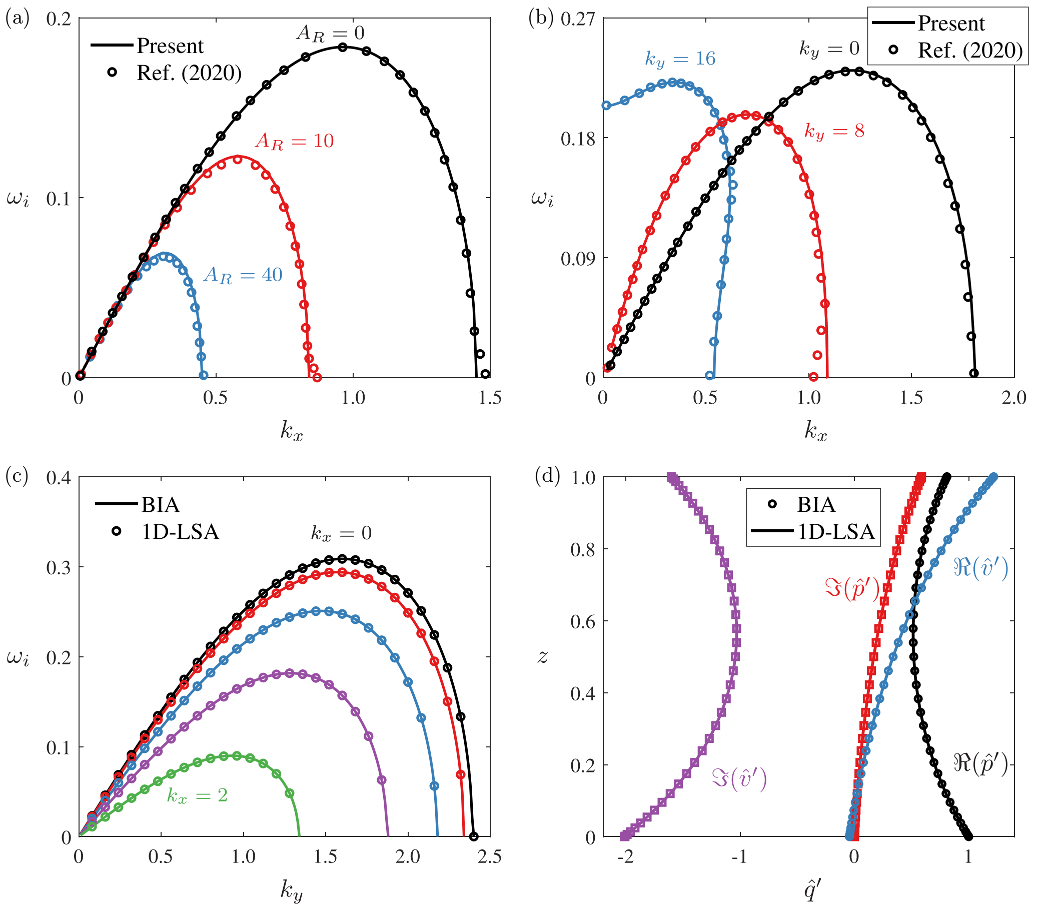

FIG. 21. Upper row: Growth rates at different (a) aspect ratios ($\mathrm{Ri} = 0$, $k_y = 0$) and (b) meridional wave numbers ($\mathrm{Ri} = 0.92$, $A_R = 0$) in the case by Zemskova *et al.* [41]. Lower row: (c) Growth rates with different k_x (0, 0.5, 1.0, 1.5, 2.0) and (d) the shape function of the $k_x = 2$ mode ($k_y = 0.96$) from BIA and 1D-LSA for the $r_z = 0$ case. Here $\Im$ denotes the imaginary part of complex.

$\bar{B} = z - y/\mathrm{Ri}$. The comparisons using 1D-LSA are shown in Fig. 21, where good agreement with the reference data is obtained. The BIA solver is verified in Fig. 21 by comparing with 1D-LSA for the modes of various zonal wave numbers. Note that the horizontal domain size is extended to 4π,

TABLE II. Growth rates of three representative modes in Sec. IV using different grid numbers.

$N = N_x = N_z$	ω_i ($r_z = 0.5$, $k_y = 2.41$)	ω_i ($r_x = 1$, $k_y = 2.42$)	ω_i ($r_x = 1$, $k_y = 3.85$)
21	0.395287	0.511875	0.209495
31	0.395319	0.511586	0.114699
41	0.395323	0.511585	0.086017
51	0.395323	0.511584	0.085278
61	0.395323	0.511584	0.085275
71	0.395323	0.511584	0.085275

so the available gap of k_x is reduced to 0.5 to allow comparisons of more modes. Both the growth rates and shape functions of various modes match well between the two solvers.

Due to the high cost of BIA, a grid-independence study is essential to determine the required grid density. Table II summarizes the results for three representative modes in Sec. IV. The first is the most unstable Phillips mode in the 1D $r_z = 0.5$ case (see Fig. 8). Using $N = N_x = N_z = 41$ is sufficient for a grid-independent growth rate with six significant digits. The second is for the 2D velocity case $r_x = 1$ (Fig. 11). The required grid number for the most unstable mode increases to 51 due to the strong zonal shear. When the mode approaches the short-wave cutoff, ageostrophic terms begin to increase, so more grid points are needed. For the third mode in Table II, $N = 61$ is required.

[1] C. Wunsch and R. Ferrari, Vertical mixing, energy, and the general circulation of the oceans, Annu. Rev. Fluid Mech. **36**, 281 (2004).

[2] Z. Zhang, W. Wang, and B. Qiu, Oceanic mass transport by mesoscale eddies, Science **345**, 322 (2014).

[3] R. Salmon, Baroclinic instability and geostrophic turbulence, Geophys. Astrophys. Fluid Dynam. **15**, 167 (1980).

[4] R. Ferrari and C. Wunsch, Ocean circulation kinetic energy: Reservoirs, sources, and sinks, Annu. Rev. Fluid Mech. **41**, 253 (2009).

[5] G. Boccaletti, R. Ferrari, and B. Fox-Kemper, Mixed layer instabilities and restratification, J. Phys. Oceanogr. **37**, 2228 (2007).

[6] J. G. Charney, The dynamics of long waves in a baroclinic westerly current, J. Atmos. Sci. **4**, 136 (1947).

[7] E. T. Eady, Long waves and cyclone waves, Tellus **1**, 33 (1949).

[8] N. A. Phillips, Energy transformations and meridional circulations associated with simple baroclinic waves in a two-level, quasi-geostrophic model, Tellus **6**, 274 (1954).

[9] J. G. Charney and M. E. Stern, On the stability of internal baroclinic jets in a rotating atmosphere, J. Atmos. Sci. **19**, 159 (1962).

[10] J. Pedlosky, The stability of currents in the atmosphere and the ocean: Part I, J. Atmos. Sci. **21**, 201 (1964).

[11] P. H. Stone, On non-geostrophic baroclinic stability: Part II, J. Atmos. Sci. **27**, 721 (1970).

[12] T. Tokioka, Non-geostrophic and non-hydrostatic stability of a baroclinic fluid, J. Meteorol. Soc. Jpn. **48**, 503 (1970).

[13] M. J. Molemaker, J. C. McWilliams, and I. Yavneh, Baroclinic instability and loss of balance, J. Phys. Oceanogr. **35**, 1505 (2005).

[14] X. Capet, J. C. McWilliams, M. J. Molemaker, and A. F. Shchepetkin, Mesoscale to submesoscale transition in the California current system. Part I: Flow structure, eddy flux, and observational tests, J. Phys. Oceanogr. **38**, 29 (2008).

[15] P. Wang, J. C. McWilliams, and C. Ménesguen, Ageostrophic instability in rotating, stratified interior vertical shear flows, J. Fluid Mech. **755**, 397 (2014).

[16] B. Qiu, Seasonal eddy field modulation of the North Pacific subtropical countercurrent: TOPEX/Poseidon observations and theory, J. Phys. Oceanogr. **29**, 2471 (1999).

[17] K. S. Smith, The geography of linear baroclinic instability in Earth's oceans, J. Mar. Res. **65**, 655 (2007).

[18] L. Feng, A. Liu, C. and Köhl, D. Stammer, and F. Wang, Four types of baroclinic instability waves in the global oceans and the implications for the vertical structure of mesoscale eddies, J. Geophys. Res. Oceans **126**, e2020JC016966 (2021).

[19] N. Nakamura, Scale selection of baroclinic instability: Effects of stratification and nongeostrophy, J. Atmos. Sci. **45**, 3253 (1988).

[20] R. Tulloch, J. Marshall, C. Hill, and K. S. Smith, Scales, growth rates, and spectral fluxes of baroclinic instability in the ocean, J. Phys. Oceanogr. **41**, 1057 (2011).

[21] V. Theofilis, Advances in global linear instability analysis of nonparallel and three-dimensional flows, Prog. Aeosp. Sci. **39**, 249 (2003).

[22] V. Theofilis, Global linear instability, Annu. Rev. Fluid Mech. **43**, 319 (2011).

[23] X. B. Shi and L. P. Røed, Frontal instabilities in a two-layer, primitive equation ocean model, J. Phys. Oceanogr. **29**, 948 (1999).

[24] J. C. McWilliams, M. J. Molemaker, and E. I. Olafsdottir, Linear fluctuation growth during frontogenesis, J. Phys. Oceanogr. **39**, 3111 (2009).

[25] J. A. Barth, Short-wave length instabilities on coastal jets and fronts, J. Geophys. Res. Oceans **99**, 16095 (1994).

[26] C. Snyder, Stability of steady fronts with uniform potential vorticity, J. Atmos. Sci. **52**, 724 (1995).

[27] M. S. Lozier, M. S. C. Reed, and G. G. Gawarkiewicz, Instability of a shelfbreak front, J. Phys. Oceanogr. **32**, 924 (2002).

[28] K. H. Brink, Baroclinic instability of an idealized tidal mixing front, J. Mar. Res. **70**, 661 (2012).

[29] E. R. Johnson and J. T. Rodney, Spectral methods for coastal-trapped waves, Cont. Shelf Res. **31**, 1481 (2011).

[30] T. Cromwell, Circulation in a meridional plane in the central equatorial Pacific, J. Mar. Res. **12**, 196 (1953).

[31] W. S. Kessler, The circulation of the eastern tropical Pacific: A review, Prog. Oceanogr. **69**, 181 (2006).

[32] J. Li and J. Gan, Characteristics and formation of the Luzon Undercurrent in the Western North Pacific: Observational study, J. Geophys. Res. Oceans **127**, e2022JC018968 (2022).

[33] B. Qiu and R. Lukas, Seasonal and interannual variability of the north equatorial current, the Mindanao current, and the Kuroshio along the Pacific western boundary, J. Geophys. Res. Oceans **101**, 12315 (1996).

[34] J. Li and J. Gan, On the formation dynamics of the North Equatorial Undercurrent, J. Phys. Oceanogr. **50**, 1399 (2020).

[35] D. Hu, S. Hu, L. Wu, L. Li, L. Zhang, X. Diao, Z. Chen, Y. Li, F. Wang, and D. Yuan, Direct measurements of the Luzon undercurrent, J. Phys. Oceanogr. **43**, 1417 (2013).

[36] J. Gan, Z. Liu, and C. R. Hui, A three-layer alternating spinning circulation in the South China Sea, J. Phys. Oceanogr. **46**, 2309 (2016).

[37] J. Gan, H. Kung, Z. Cai, Z. Liu, C. Hui, and J. Li, Hotspots of the stokes rotating circulation in a large marginal sea, Nat. Commun. **13**, 2223 (2022).

[38] G. K. Vallis, *Atmospheric and Oceanic Fluid Dynamics: Fundamentals and Large-scale Circulation* (Cambridge University Press, Cambridge, UK, 2006).

[39] T. R. Bewley and S. Liu, Optimal and robust control and estimation of linear paths to transition, J. Fluid Mech. **365**, 305 (1998).

[40] R. Plougonven, D. J. Muraki, and C. Snyder, A baroclinic instability that couples balanced motions and gravity waves, J. Atmos. Sci. **62**, 1545 (2005).

[41] V. E. Zemskova, P.-Y. Passaggia, and B. L. White, Transient energy growth in the ageostrophic Eady model, J. Fluid Mech. **885**, A29 (2020).

[42] P. J. Schmid and D. S. Henningson, *Stability and Transition in Shear Flows* (Springer, New York, 2001).

[43] E. Heifetz and B. F. Farrell, Generalized stability of nongeostrophic baroclinic shear flow. part I: Large Richardson number regime, J. Atmos. Sci. **60**, 2083 (2003).

[44] X. Chen, L. Wang, and S. Fu, Energy transfer of hypersonic and high-enthalpy boundary layer instabilities and transition, Phys. Rev. Fluids **7**, 033901 (2022).

[45] K. S. Smith, Eddy amplitudes in baroclinic turbulence driven by nonzonal mean flow: Shear dispersion of potential vorticity, J. Phys. Oceanogr. **37**, 1037 (2007).

[46] G. Roullet, J. C. McWilliams, X. Capet, and M. J. Molemaker, Properties of steady geostrophic turbulence with isopycnal outcropping, J. Phys. Oceanogr. **42**, 18 (2012).

[47] X. Capet, G. Roullet, P. Klein, and G. Maze, Intensification of upper-ocean submesoscale turbulence through Charney baroclinic instability, J. Phys. Oceanogr. **46**, 3365 (2016).

[48] P. Klein, B. L. Hua, G. Lapeyre, X. Capet, S. Le Gentil, and H. Sasaki, Upper ocean turbulence from high-resolution 3D simulations, J. Phys. Oceanogr. **38**, 1748 (2008).